

# Geophysical characterization of the El Cervunal kame complex (Sierra de Gredos, Iberian Central System): Insight of infill geometry and reconstruction of former glacial formations

José Luis Granja-Bruña<sup>a,\*</sup>, Valentí Turu<sup>b,c</sup>, Rosa M. Carrasco<sup>c</sup>, Alfonso Muñoz-Martín<sup>a,d</sup>, Xavier Ros<sup>b</sup>, Javier Fernández-Lozano<sup>e</sup>, Rodrigo L. Soteres<sup>f,g</sup>, Theodoros Karampaglidis<sup>h</sup>, José Antonio López-Sáez<sup>i</sup>, Javier Pedraza<sup>a</sup>

<sup>a</sup> Department of Geodynamics, Stratigraphy and Paleontology, Complutense University, C/José Antonio Novais 12, 28040 Madrid, Spain

<sup>b</sup> Fundacio Marcel Chevallier, Edifici Socio-Cultural la Llacuna, AD500 Andorra la Vella, Andorra

<sup>c</sup> Department of Geological and Mining Engineering, Castilla-La Mancha University, Avda. Carlos III, s/n, 45071 Toledo, Spain

<sup>d</sup> Instituto de Geociencias – IGEO (UCM, CSIC), C/José Antonio Novais 12, 28040 Madrid, Spain

<sup>e</sup> Higher Technical School of Mining Engineering, Campus de Vegazana s/n, 24071 León, Spain

<sup>f</sup> Instituto de Geografía, Pontificia Universidad Católica de Chile, Avda. Vicuña Mackenna, 4860 Santiago, Chile

<sup>g</sup> Millennium Nucleus Paleoclimate, ANID Millennium Science Initiative, Santiago, Chile

<sup>h</sup> MONREPOS, Archaeological Research Centre and Museum for Human Behavioural Evolution, Schloss Monrepos, 56567 Neuwied, Germany

<sup>i</sup> Environmental Archaeology Research Group, Institute of History, CSIC, Albasanz 26-28, 28037 Madrid, Spain

## ARTICLE INFO

### Keywords:

Vertical electrical sounding (VES)  
Electrical resistivity tomography (ERT)  
Seismic tomography  
Refraction microtremor (ReMi)  
Magnetic resonance sounding (MRS)  
Kame-moraine  
Former glacial reconstruction  
Iberian Central System

## ABSTRACT

Geological and geophysical studies in complex valley troughs provide a key record for the reconstruction of paleoenvironmental conditions during the Quaternary. Here we present a study of the sedimentary infill of the El Cervunal kame complex or El Cervunal trough (Sierra de Gredos, Iberian Central System) by means of a combined interpretation of near-surface geophysical techniques supported by geomorphological and borehole data. A set of 1D and 2D near-surface geophysical methods, including electrical (Vertical Electrical Sounding and 2D Electrical Resistivity Tomography), seismic (2D Seismic Tomography and 1D Refraction Microtremor) and Magnetic Resonance Sounding techniques, were used to test their applicability in providing better insight on the infill nature and geometry. Because of greater sensitivity and higher resolution and coverage achieved with resistivity methods, the electrical resistivity has proven to be the most informative physical parameter, while seismic and magnetic resonance methods were complementary. The sedimentary infill was classified into three geophysical units and five sub-units with their geological interpretation. Unit 1 consists of a postglacial sedimentary sequence and includes alluvial-plain and alluvial-fan deposits. Units 2 and 3 below the postglacial unit were interpreted as glacial sequences including kame (glacigenetic and fluvio-glacial) and morainic deposits, respectively. Subsoil information combined with the geomorphological data enabled the partial reconstruction of the map-view geometry of the morainic bodies at the El Cervunal trough. The results suggest a complex evolution of the study area where erosive-sedimentary processes dominate, but also structural factors should be considered. At least five well-differentiated stages can be established to explain the occurrence of the trough infill: pre-glacial, maximum glacial extension, trough obturation, glacial retreat and periglacial-postglacial.

## 1. Introduction

The application of combined geophysical techniques to elucidate the geometry, stratigraphy and nature of the sedimentary infill in complex valley troughs, depressions or paleovalleys, is a generalized procedure in

many geomorphological studies (e.g., Schrott et al., 2003; Kruse, 2013; Colombero et al., 2014; Bottari et al., 2017; Rubio Sánchez-Aguililla et al., 2017). In the Iberian Central System (hereinafter ICS), this methodological approach was first conducted only a few years ago to assess the characteristics of the depressions associated with the ancient

\* Corresponding author.

E-mail address: [jlgranja@ucm.es](mailto:jlgranja@ucm.es) (J.L. Granja-Bruña).

<https://doi.org/10.1016/j.jappgeo.2021.104478>

Received 23 October 2020; Received in revised form 19 August 2021; Accepted 18 October 2021

Available online 23 October 2021

0926-9851/© 2021 The Author(s).

Published by Elsevier B.V. This is an open access article under the CC BY-NC-ND license

(<http://creativecommons.org/licenses/by-nc-nd/4.0/>).

glaciers (i.e., paleoglaciers) of the Upper Pleistocene (Carrasco et al., 2015a). These sites (locally termed “navas”) have traditionally been studied to reconstruct the palaeoecological conditions in the ICS during the Quaternary, contributing to expand our knowledge regarding the evolution of the former environmental conditions at a regional and hemispheric scale (e.g., López-Sáez et al., 2014, 2020).

The combined and integrated interpretation of distinct geophysical methods, properly constrained with geological observations and other subsoil data, makes it possible to interpret the bedrock and infill geometries as well as to infer the presence of fluids (e.g., Butler, 2005; Reynolds, 2011; Everett, 2013). The geophysical interpretation is based on the analysis of vertical and lateral distribution of maxima, minima, and gradients of physical parameters like electrical resistivity or seismic velocity. Vertical Electrical Sounding (VES) and 2D Electrical Resistivity Tomography (ERT) are widely used techniques with which to measure the vertical and/or the lateral distribution of apparent resistivity of the subsoil (e.g., Cardarelli and De Donno, 2019 and references therein). The initial apparent resistivity and the electrode spacing are inverted to obtain a 1D and/or 2D model of true resistivity vs. depth that can be interpreted in geo-electrical terms (Zohdy, 1989). Near-surface seismic methods have a broad range of applications in geotechnical or environmental studies (e.g., Milsom and Eriksen, 2011; Everett, 2013). P-wave active seismic refraction methods (ST) are often used to study the geometry and sedimentary basin infill (e.g., Turu, 1999; Turu et al., 2007; Yamakawa et al., 2012). By measuring the travel time of direct and critically refracted P-waves and using inversion tomographic techniques, it is possible to obtain a depth-section with P-wave velocity distribution (i.e., 2D velocity model) that can be interpreted in terms of seismic layers. This methodology shows limitations where there are significant levels of energy absorption and attenuation (Reynolds, 2011), but it can be partially compensated by using surface wave methods like the Refraction Microtremor seismic method (ReMi). The ReMi method uses the dispersion of the Rayleigh waves generated by ambient noise and/or active sources to get an in-depth 1D Rayleigh wave velocity ( $V_R$ ) model (Louie, 2001). In addition, Magnetic Resonance Sounding (MRS) is a technique commonly used in hydrogeology for groundwater surveying because it is the only geophysical method that detects the existence, amount and productiveness of groundwater in the subsoil from the surface (e.g., Plata and Rubio, 2008; Yaramanci and Hertrich, 2009). This method is based on energizing the subsoil with an increasing electromagnetic pulse generated in a square loop antenna. Gradually increasing the magnetic field excitation allows the investigation depth to be increased. When the pulse stops, the subsoil response is recorded by three parameters (i.e., initial amplitude, decay time and phase) which by means of 1D inversion can be directly related to the amount of water and the hydraulic permeability (Legchenko and Valla, 2002).

Earlier studies based on geophysical techniques in the ICS troughs showed clear limitations in coverage, resolution, and depth. The sedimentary infill was only analyzed up to 3–6 m of depth, revealing mainly homogeneous sedimentary characteristics (comprising often only two distinct sedimentary sequences) that were not pre-Holocene in age (e.g., López-Sáez et al., 2014). However, previous investigations applying a combined geological and geophysical approach have proven to be more effective in understanding the 3D geometry of the trough infill. They provide constraints to better plan mechanical drillings sites and to obtain a more complete sedimentary record for genetic, environmental and chronological interpretations. For instance, this type of procedure was applied in the Navamuño depression (Sierra de Béjar, ICS; Carrasco et al., 2018) confirming the effectiveness of this methodological approach in depressions that had initially been analyzed with very limited results. In Navamuño depression three main geoelectric layers (G1, G2 and G3) were recognized. The analyzed infill was up to 20 m of depth according to borehole sounding and aged from ~800 cal yr BP (at depth 1.11 m) to ~16,800 cal yr BP (at depth 15.90–16.0 m). Its sedimentary record allowed the interpretation of the local environmental

changes during the late glacial stages (i.e., from the Older to the Younger Dryas) and postglacial stage (Holocene) (Carrasco et al., 2015a, 2015b, 2018; Turu et al., 2018; López-Sáez et al., 2020). In addition, these works have made it possible to adjust the glacial chronologies based on cosmogenic dating as a basis for establishing a more adjusted production rate and correlation with other areas, especially the Mediterranean mountains (Braucher et al., 2013).

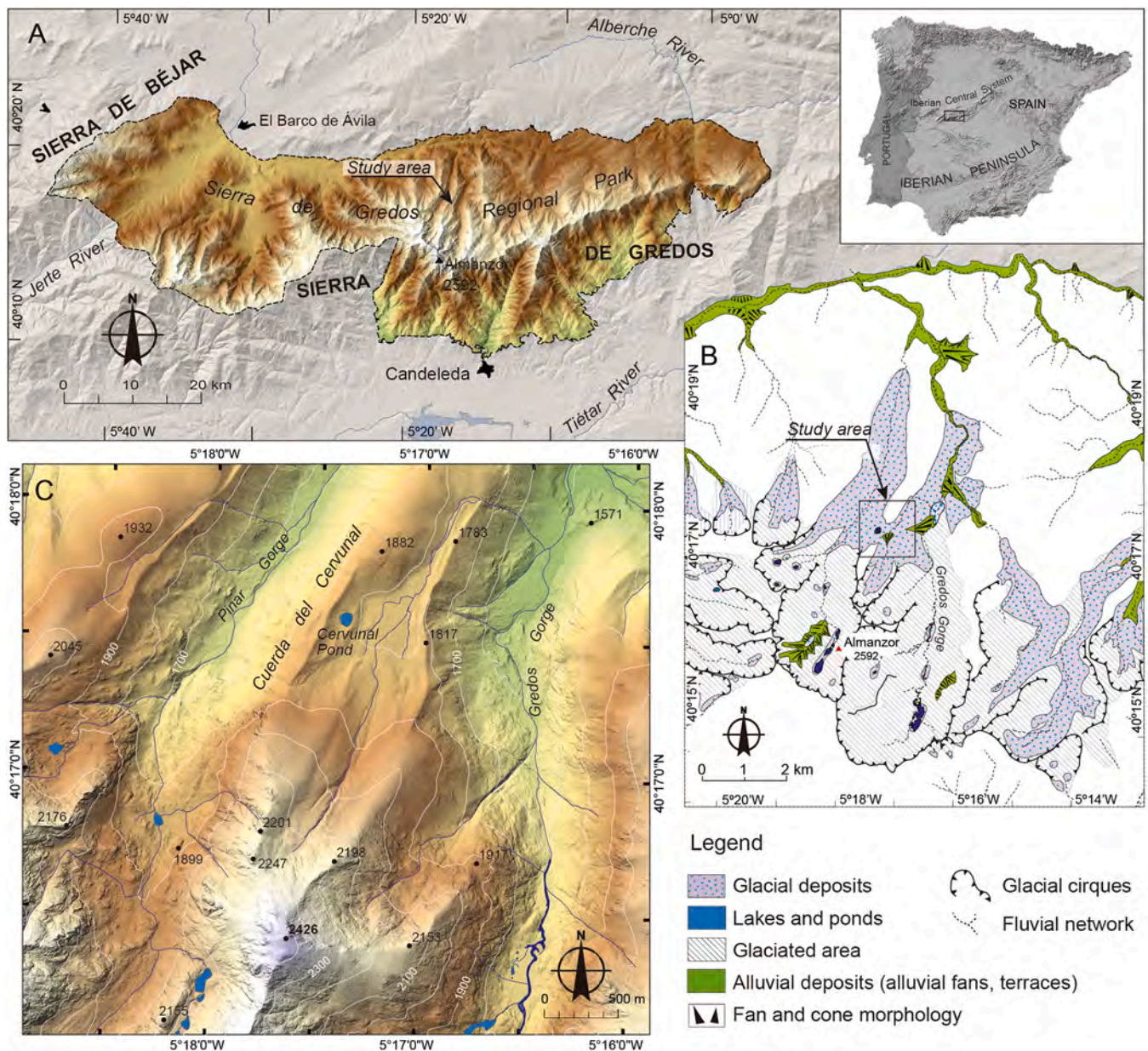
This study aims to apply a similar approach to that carried out in Navamuño depression in order to explore the subsoil of the El Cervunal kame complex or the El Cervunal trough (Sierra de Gredos, ICS), and to acquire insight on the geometry, nature and genetic context of its sedimentary record (Fig. 1). This approach is scientifically reasonable because of the remarkable similarities between Navamuño and El Cervunal: both are in the ICS, located on a densely fractured granitic substrate, and sharing similar genesis and evolution involving tectonic, glacial, fluvio-glacial and slope processes (Carrasco et al., 2018, 2020). Therefore, this study of the El Cervunal trough will contribute to expand the first insights from Navamuño to a reference model that can be generalized to other troughs and depressions across the whole ICS. Considering the geomorphological and geological setting of the El Cervunal flat plain, we have selected a set of feasible 1D and 2D near-surface geophysical methods to test their applicability based on a good balance between resolution and penetration. We have used resistivity techniques (1D/2D VES and 2D ERT), surface seismic methods (2D ST and 1D ReMi) and 1D MRS. Most of these geophysical methods have been tested in other mountain systems with similar purposes (e.g., in the Pyrenees: Vilaplana and Casas, 1983; Bordonau, 1992; Turu, 1999; Turu et al., 2007; Pélachs et al., 2011; Rubio Sánchez-Aguillilla et al., 2017; in the Iberian Central System: Turu et al., 2018; Carrasco et al., 2018; and in the Alps; van Rensbergen et al., 1998, 1999; Reitner et al., 2010).

## 2. Regional setting

The El Cervunal kame complex or trough (hereinafter CvT) is located on one of the plateaus of the central sector of the Sierra de Gredos (Fig. 1). The central sector of this range hosts the highest mountains of the ICS with peaks above 2400 m. The range's highest mountain is Pico Almanzor (2492 m asl). The ICS is an intraplate mountain system formed during the Alpine orogeny (mainly during the Miocene–Pliocene) by the uplift of the Hercynian or Variscan basement (e.g., De Vicente et al., 2018). This gave rise to a stairway morphostructure determined by fault-bounded blocks (piedmonttreppe or piedmont benchland Penckian model; see Pedraza, 1994).

The plateaus in this topographic structure correspond to ancient peneplains with an extensive area of weathered materials (Molina-Balasteros et al., 1997) and some minor depressions and fracture corridors originated during the first stages of mountain building reactivation. Some of these ancient depressions (essentially from the Palaeogene) have conditioned the location and development of several recent fluvial, glacial and lacustrine processes (Carrasco et al., 2018; Turu et al., 2018). The regional morphostructural indicators allowed to correlate CvT with the series of intramontane depressions and paleovalleys originating during the Cenozoic that are responsible for the configuration of its current relief (Pedraza, 1994; De Vicente et al., 2018; Carrasco et al., 2018; Cunha et al., 2019). A complex evolutive history from its origins in the Late Variscan (Hercynian) enlarges subsidence processes during the Quaternary, although their tectonic significance is still under discussion (Carrasco and Pedraza, 1991; Villamor et al., 2012; De Vicente et al., 2018; Carrasco et al., 2018). The lithology at CvT corresponds to two major geological formations, the Variscan basement and the Quaternary sedimentary cover. The first is represented by Late-Variscan granitoids (i.e., monzogranites, granodiorites; GEODE, 2004), the second by surficial deposits due to glacial and flooding processes and, to a lesser extent, periglacial and fluvial ones.

Chronological data based on Terrestrial Cosmogenic Nuclide (TCN) surface exposure dating from several sites across the Sierra de Gredos



**Fig. 1.** Location of the study area. A) Sierra de Gredos regional park (see inset map for location in the Iberian Peninsula). B) Regional geomorphology of the study area (modified from Carrasco et al., 2020). C) Digital elevation model showing an enlarged view of the El Cervunal trough (see Fig. 1B for location).

present a glacial history in this area which can be summarized into three stages (Palacios et al., 2011, 2012; Domínguez-Villar et al., 2013; Pedraza et al., 2013; Oliva et al., 2019): i) The Glacial Maximum from ~26–24 to ~20 ka BP; ii) the stage of readvance and stabilization from ~20 to ~17 ka BP; and iii) the stage of deglaciation between ~17 and ~14 ka BP. At the regional scale, these three evolutionary stages of glaciers are indicated by three morpho-stratigraphic formations called, from older to younger (Pedraza et al., 2013; Carrasco et al., 2015b; Oliva et al., 2019): Peripheral Deposits (PD), Principal Moraine (PM) and Internal Deposits (ID).

The fine grain-size sediments and fluvial deposits are associated with glacial stages, post-glacial and present-day environments. At the bottom of the CvT these paraglacial processes form the plain created by the sediment overflowing in former lacustrine basins or similar depressions. At the trough sides thick morainic deposits are sedimented by glaciers, overflowing depressions with kame deposits that are mostly glaci-fluvial- and glaci-lacustrine-like. The flat surfaces of marginal

kame terrasses and the bottom of the trough are occupied by hydro-morphic soils, currently colonized by herbaceous vegetation (*Nardus stricta* and *Festuca indigesta*) forming grasslands or meadows locally termed as “Cervunales” or “Navas”. The moraines, the flat plain meadows and the granite slopes are the main relief elements in this area (Martínez de Pisón and Muñoz-Jiménez, 1972; Martínez de Pisón and Palacios, 1997; Pedraza and Carrasco, 2005).

According to the available climatological data (AEMET/IMPA, 2011), the study area is characterized by a continental Mediterranean mountain climate. The average minimum temperature of the coldest month is <0 °C, and the average maximum temperature of the hottest month is >15 °C. Average annual rainfall is >1700 mm, with snowfall between the months of November and May at altitudes of over 1900 m asl, which implies the existence of an altitudinal band with an attenuated seasonal periglacial environment.

### 3. Data and methods

The methodology of this study combines different geophysical techniques supported by geomorphological observations and borehole data to study the geometry, stratigraphy and nature of the sedimentary infill. Combining and integrating the geophysical models based on independent physical parameters such as resistivity and seismic velocity, when reasonable numeric coherence exists, allow to obtain a valuable information about the subsoil (e.g., Kvamme et al., 2019). Moreover, when this indirect subsurface information is integrated and validated with geological outcrops, geomorphology and borehole data, it is

possible to decrease uncertainty and reach robust approximations of the subsoil geology (e.g., Reynolds, 2011; Milsom and Eriksen, 2011; Everett, 2013). Geological and geophysical data were acquired during two field surveys carried out in July and September of 2017.

#### 3.1. Geomorphology

Most of the available information on the geology and geomorphology of the CvT, including substrate lithology, glacial morphology and chronology, appears in general studies of the Sierra de Gredos (Martínez de Pisón and Muñoz-Jiménez, 1972; Ruiz and



**Fig. 2.** Field work and data acquisition. A) Geophysical and borehole data location. VES = Vertical Electrical Sounding. SS = Seismic Sounding (Surface Seismic Tomography and Refraction Microtremor). ERT = Electrical Resistivity Tomography. MRS = Magnetic Resonance Sounding. S1 = Borehole. DPSH = Dynamic Probing Super Heavy sounding. Dashed pink line shows the VES pseudo-cross-section of Fig. 5. B) Transportation of the geophysical and borehole equipment by helicopter (the study area is 2–3 h trekking from nearest transitable road by car). C) ERT acquisition. D) SS acquisition. E) S1 Borehole and DPSH test. (For interpretation of the references to colour in this figure legend, the reader is referred to the web version of this article.)

Gabalión, 1981; Acaso, 1983; Martínez de Pisón and Palacios, 1997; Pedraza and Carrasco, 2005; Palacios et al., 2011, 2012; Pedraza et al., 2013; Oliva et al., 2019). Therefore, references to CvT are scarce and do not contain specific data on the geometry, surficial deposits, or genetic content of this kame complex. There are only two papers providing partial data for this site. The first is a paleopalynology study based on a 3 m-long borehole core sample (Ruiz-Zapata and Acaso-Deltell, 1981), and the second is a detailed inventory of the glacial landforms of High Gredos Massif area which includes the CvT (Carrasco et al., 2020). This second work is part of a recently initiated series of investigations in this area, which include conducting new geological mapping from vertical aerial photographs (Scale 1:10000 and 1:18000) and PNOA-2014 orthophotos (Instituto Geográfico Nacional, [www.ign.es](http://www.ign.es)). The results of this regional study together with our detailed outcrop observations during field surveys have served as the basis to define the geological and geomorphological units presented in this study.

### 3.2. Borehole data

In order to have a preliminary estimation of the thickness and nature of the sedimentary layers before drilling, we performed a Dynamic Probing Super Heavy (DPSH) sounding in the southern area of the CvT (DPSH in Fig. 2A and E). This dynamic test consists of driving a cone-shaped rod into the ground using a hammer, with a regular drop height. The instrumentation, test procedure and the data processing were carried out following the approach by Turu et al. (2018) and references therein. This method provides the strength value of the sedimentary strata, or the ultimate pressure to break the tested soil, named as Qd. The DPSH test was stopped at 1280 cm of depth, where the hammering number were > 100 per 20 cm of penetration, because of excessive ground resistance to this method. After the DPSH test, a 1280 cm-deep borehole was drilled for a direct observation of the subsoil, (S1 in Fig. 2A and E). The coring device consisted of a piston sampler pushed by a dynamic penetrometer system (Turu et al., 2018). This device allowed the collection of 11 samples in a steel core of Ø43 mm and 1.5 m of length. Because of the cohesionless behavior and coarse grain-size of the sediments (mostly gravels) only spot samples were collected at the intervals 385–405 cm, 700–840 cm and 1040–1280 cm. The core description was carried out in situ and completed later in the laboratory.

### 3.3. Geophysical methods

The first geophysical survey consisted of an initial prospecting of the CvT area using VES to gather a preliminary understanding of the sediment infill and to identify better areas for future data acquisition (VES in Fig. 2A). The second survey consisted of a larger deployment of geophysical and borehole helitransported instrumentation (Fig. 2B). Geophysical instrumentation included ERT, ST, ReMi and MRS methods (Fig. 2A, C and D).

#### 3.3.1. Resistivity methods

**3.3.1.1. Vertical Electrical Sounding (VES).** Six VES (VES-1 to VES-6) were acquired along the axial zone of the CvT using a Kalenov-500 prototype resistivity meter (Fig. 2A). Electrode array was deployed following a Schlumberger-type configuration, increasing the MN spacing from 0.5 m to 2 m when measure resolution was insufficient, and a maximum AB/2 spacing of 100 m (App. A). The electrode array was oriented N-S following the elongated dimension of the plain, except for VES-6 that was deployed E-W. VES field data were inverted by means of commercial IX1D software, obtaining a 1D resistivity model and corresponding equivalence analysis that allows a quantitative assessment (App. A). The maximum investigation depth was 25 m and apparent resistivity values between 12,000 and 700  $\Omega\cdot\text{m}$ . Lateral correlation of 1D models derived from the VES inversion made it possible to

build a pseudo cross-section of resistivity data using the IPI2Win free-ware (Bobachev et al., 2003). The VES methodology is more appropriate when the variation in resistivity is significant at depth and small laterally. In the case of the CvT, the heterogeneous lithology yields uncertainty in the VES data that needs to be assessed by electrical equivalence analysis and finally reduced by the integration of other geophysical methods and geological data.

**3.3.1.2. 2D Electrical Resistivity Tomography (ERT).** In this study 2D ERT data were collected using a RESECS DMT multi-electrode resistivity meter with 5 m-electrode spacing. Four profiles were recorded with lengths from 150 m (31 electrodes; ERT-4 in Fig. 2A) to 315 m (64 electrodes; ERT-1 in Fig. 2A). Profiles ERT-2 and ERT-3 were integrated and combined with an overlap of 80 m resulting in the composed profile ERT-2/3 with an effective length of 395 m (equivalent to 80 electrodes; ERT-2/3 in Fig. 2A). Profiles were arranged to record data along and across the CvT. Several electrode configurations were tested during the acquisition (e.g., Schlumberger, Schlumberger-Wenner, Dipole-Dipole). However, only reasonable signal-to-noise ratios (SNR) were obtained with Wenner and Wenner-Schlumberger configurations, reaching a maximum investigation depth of 40 m for sections ERT-1 and ERT-2/3, and 25 m for the section ERT-4 (App. B). The acquisition software allowed an iterative quality assurance and control (QA/QC) during the acquisition procedure, repeating each failed or out-of-range measurement until acceptable measures are obtained. The final field dataset showed good quality with average measurement errors below 1%. The commercial RES2DINV software was used for field data inversion including topography (Loke et al., 2013 and references therein). A regular inversion algorithm using a 4-node distorted finite-element grid was used so that the surface of the grid matches the topography. The minimum size of the elements was the same as the electrode spacing (5 m). Data errors were systematically excluded during the acquisition and inversion procedures. During the inversion workflow, we carried out a subsurface sensitivity calculation to detect any potential anomalous variations with depth and location (App. B). The 2D resistivity models gave numerical coherence after 6 iterations (RMS on last two iterations was below 5% and average absolute error below 7%).

#### 3.3.2. Seismic methods

**3.3.2.1. 2D Surface Seismic Tomography (ST).** 2D ST data were collected using a DAQ-Link II 24-channel and 24-bit seismometer and a multi-channel array of 4.5 Hz geophones. The seismic deployment consisted of two 115 m-long profiles with 5 m-geophone spacing and source interval between 20 and 30 m (SS-1 and SS-2 in Fig. 2A). The signal was recorded with 2 ms-interval sampling and a 1 s of acquisition window. The seismic source location was at end-on forward and reverse shots points and two or three intermediate split-spread shot points. The seismic waves were generated by percussion with a 6 kg hammer on a metal plate placed on the ground. Field interactive signal QA/QC, pre-processing, and pick arrivals was carried out with VibraScope freeware (Seismic Source Co., [seismicsource.com](http://seismicsource.com)). Signal QA/QC consisted of quantitatively evaluating the shot gathers (i.e., standard frequency filtering, automatic-gain control and equalizing to enhance the signal traces) to better identify the first P-wave arrivals and then to repeat the shot as necessary to get a minimum of three good quality shot gathers that are finally stacked (App. C). Repeating measurements was a frequent procedure because the soft soil conditions of the experiment site with peat and low-compacted soil yielded a significant absorption and attenuation of the seismic signal.

P-wave first arrivals travel times and offset distances were imported in commercial Rayfract software to perform an inversion based on a 2D forward modelling tomographic procedure. This software uses an optimized wave-path eikonal travel-time inversion (WET, Schuster and Quintus-Bosz, 1993). The forward modelling was addressed in parallel

from two starting models: DeltaV and Uniform Gradient. After 20 inversion iterations both models show similar results with good numerical coherence and RMS errors below 3%. Inversion QC was accomplished by ray-tracing coverage to identify less covered regions and possible inversion artefacts (App. D). Inversion results provided 2D P-wave velocity models reaching maximum depths of 20 m.

**3.3.2.2. 1D Refraction Microtremor (ReMi).** As mentioned in the regional setting, the CvT is covered by an average 1 m-thick low-compacted layer of soil that yields a significant absorption and attenuation of the P-wave seismic signal in the active seismic experiment (App. C). Thus, to compensate this energy loss in P-wave and to test the applicability of the active experiment, we used the ReMi method based on surface wave dispersion, which has a significant lower absorption coefficient (e.g., Everett, 2013). The ReMi acquisition procedure consisted in using a multichannel geophone array to measure the natural and/or artificial seismic signals. In the CvT, data were collected along two profiles using the same seismometer and geophone array as for 2D ST (SS-1 and SS-2 in Fig. 2A). In this case the sampling rate was also 2 ms but the acquisition window was 30 s-long. The seismic source was natural noise, the percussion with a 6 kg hammer along the geophone array and the signal generated by a DPSH system. Signal QA/QC consisted of visual analysis and repeating the 30 s-long record for 10 times and then building a stacked signal (App. E1). This procedure allowed us to recover a part of the degraded signal yielded by the peat and low-compacted soil, while the use of percussion improved the high frequency content.

Commercial SeisOpt® ReMi™ software was used for field data inversion (Louie, 2001). The time-domain signal traces were transformed to frequency-domain and then the spectral decomposition of Rayleigh waves allows to identify the frequency and Rayleigh velocity ( $V_R$ ) of each phase-component. The spectrum of frequency vs. slowness ( $1/V$ ) shows a representation of the average ReMi Spectral Ratio (App. E2) that allows to distinguish the Rayleigh waves from other seismic events (i.e., because Rayleigh waves show a dispersive character where phase velocity decreases with higher frequencies). The picking of the spectrum following the base of the average ReMi Spectral Ratio provides a dataset of Vphase vs. period (i.e., dispersion curve, App. E3). The dispersion curve was inverted to obtain a 1D- $V_R$  model centered on the 2D geophone array deployment (App. E4). 1D- $V_R$  velocity models reaching a maximum depth of 30 m and averaged RMS error below 4%. Finally, the  $V_R$  is transformed to S-wave velocity ( $V_s$ ) assuming the standard conversion  $V_s = V_R/0.920$  (e.g., Everett, 2013).

### 3.3.3. Magnetic Resonance Sounding (MRS)

MRS data were collected using the NUMIS LITE system from Iris-Instruments with a  $60 \times 60$  m antenna (MRS in Fig. 2A). In order to cancel the random noise and improve the SNR, each electromagnetic excitation pulse was repeated several times and then stacked to reach as close as possible the instrumental noise ( $\sim 10^{-5}$  nV). Ambient electromagnetic noise was also recorded in a time lapse of 40 ms before introducing the current into the circuit. The quality of the results also depends on the amplitude and inclination of the Earth's magnetic field, magnetic susceptibility, electrical conductivity of rocks, and on natural and artificial electromagnetic noise (Legchenko and Valla, 2002). The sounding consisted of several measurements increasing the values of electromagnetic pulse ( $q$ , in A·ms) to establish the functions: initial amplitude  $E_0(q)$ , decay time  $T_2^*(q)$  and/or  $T_1^*(q)$ . The measured resonance signal is estimated to come from the existing water inside a parallelepiped or cylindrical volume with a base 1.5 times the diameter of the antenna used and maximum depth equal to this diameter (Vouillamoz et al., 2007). The inversion of field data was performed with SAMOVAR v6.2 software by IRIS Instruments and following a standard procedure (Yaramanci and Hertrich, 2007). Data used in the inversion showed an average SRN  $>1$  and external/internal noise ratio

$< 1$ . This allowed a feasible semi-quantitative interpretation (Legchenko, 2007) by means of building a 1D model of water content and permeability, and an error estimation of 34% for porosity and 24% for permeability.

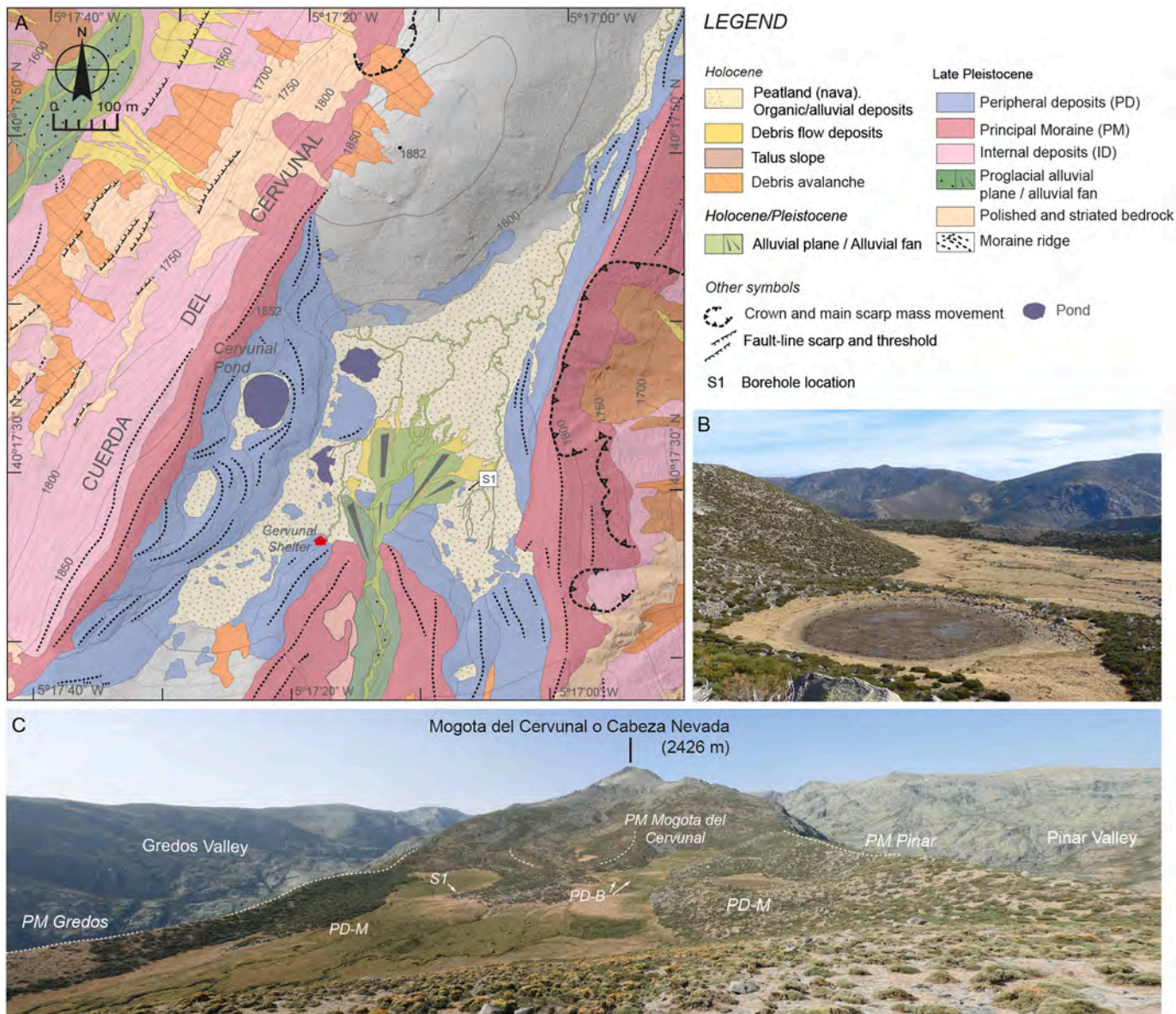
## 4. Results and interpretation

In this section we present the results of the detailed geomorphological mapping and borehole data and then the combined interpretation with geophysical data. As an approximation, the heterogeneous and heterometric lithology commonly found in glacial settings such as the CvT provides a priori good conditions to carry out a geophysical prospecting. This makes a significant contrast in physical parameters such as electrical resistivity and seismic velocities foreseeable. In addition, the CvT geomorphology provides remarkable hydrologic boundary conditions, like bedrock and moraines, that ensures enough groundwater storage for a deep MRS prospecting.

### 4.1. Geomorphology

The CvT consists of a NNE-SSW trending triangular-shaped hanged plain, confined by two moraines and large granitic hills (Fig. 3A). It is about  $0.325 \text{ km}^2$  in area, 1.7 km in length and 350 m-wide in the south and becomes progressively narrower to the north until its eastern and western limits converge to close the main plain. From a physiographic viewpoint, the CvT presents the characteristic features of "navas" in the ICS (i.e., flat, treeless, sometimes marshy ground, generally situated between elevations; Novo and Fernández Chicarro, 1949) and can be classified as a peaty-system created by sediment overfilling in a former moraine-dammed type basin (Figs. 3B and C).

The boundaries of the CvT are defined by lateral moraines of the Gredos and El Pinar paleoglaciers, the latero-frontal moraines of Cabeza Nevada paleoglacier and the granite slopes associated with fault line scarps and pre-glacial fluvial incision (Fig. 3C). The eastern boundary of the basin along its entire route and the southern half of the western boundary are clearly delimited by the NE-SW trending ridges of lateral moraines of the Gredos and Pinar paleoglaciers, respectively. The southern boundary is somewhat more complex due to the participation of granite slopes and the interference between the most external minor lateral moraines of the Gredos-Cabeza Nevada and Pinar-Cabeza Nevada paleoglacier systems. However, the main limit can be attributed to the latero-frontal moraine of the Cabeza Nevada paleoglacier. All these lateral moraines that form the main limits of CvT correspond to a morpho-stratigraphic formation termed in the ICS as "Principal Moraine (PM)", which indicates the mayor stages of readvance and stabilization of the glaciers in these areas and, in addition, the transition between the stages of expansion of the glacier and the stages of deglaciation (Pedraza et al., 2011, 2013; Oliva et al., 2019; Carrasco et al., 2020). The PM formation is associated with an accreted sequence of minor lateral moraines of Gredos and Pinar paleoglaciers. According to the chronological data obtained by  $^{36}\text{Cl}$  exposure dating, the construction of the PM formation can be established between around  $\sim 24$  ka and  $\sim 20$  ka BP (Palacios et al., 2011, 2012; Oliva et al., 2019). Within the PM formation associated with both the Gredos and El Pinar paleoglacier, older minor moraines formed by the Cabeza Nevada glacier appear attached or close to the distal slope of the PM formation, and may even overlap causing small intra-morainic lakes or ponds (Cervunal Pond in Figs. 3A and B). The moraines are composed of boulders and large boulders with a coarse-grained matrix. They are lithologically homogeneous mostly composed of granitoids and their sandy weathering products (Rubio et al., 1992). These moraines correspond to a morpho-stratigraphic formation termed in the ICS as "Peripheral Deposits (PD)", which is the indicator of the Maximum Ice Extent and a series of glacial oscillations (i.e., limited retreat and stabilizations) around the maximum. According to the chronological data obtained by  $^{36}\text{Cl}$  exposure dating, the construction of this PD formation can be established between  $\sim 26$  ka



**Fig. 3.** Geomorphology and physiography of the study area. A) Geomorphological mapping (see also Carrasco et al., 2020). Gray-shaded area shows a hill where the igneous basement outcrops. B) View from the SW of the CvT (the Cervunal Pond is in the foreground). C) View from the N of the study area. Note the three glacial systems: Gredos, Mogota del Cervunal-Cabeza Nevada and Pinar. PD-B = Peripheral Deposit-Blocks. PD-M = Peripheral Deposit-Moraine. PM = Principal Moraine. S1 = Borehole and DPSH test.

and ~24 ka BP (Palacios et al., 2011, 2012; Oliva et al., 2019). Magmatic rocks are present on the northern half of the western boundary and part of southern slopes sides of CvT (see gray-shaded area in Fig. 3A). These rocks are intrusive monzogranites and porphyritic biotite granodiorite (GEODE, 2004), with residual enclaves of metamorphic rocks (varying from micacite to nebulite-migmatite) and associated with NE-SW and NNE-SSW fractures. In the northern area, the foot-plain of the CvT is directly connected to a steep slope with a clear knickpoint slope break and the fresh-looking granitic rock. To the south, however, between the scarped slope and the foot-plain, minor intermediate deposits of glacial and fluvioglacial origin are observed and the rock substratum are partially weathered forming grus and surficial deposits (lithosols and slope deposits). The bottom of the flat plain presents hydromorphic soils and grassland developed over a complex sedimentary filling in which sequences of tills, fluvioglacial and lacustrine deposits may appear (“basal complex”, Carrasco et al., 2015b, 2020). The “basal complex” formation, as

described for other ICS areas (Carrasco et al., 2018; Turu et al., 2018), may consists of weathered granitic substrate (grus) that in some cases presents notable hydrogeological and geotechnical convergences with the sedimentary formations of the arkose cover which appear in some ICS intermountain troughs (Centeno and Brell, 1987; Molina-Ballesteros et al., 1991). The present environment includes the alluvial-fan alluvial plain, marshy areas with seasonal flooding and in some marginal areas gravitational and rill slope deposits. The origin of these formations is due to the processes developed in an attenuated periglacial environment characteristic of a Mediterranean mountain climate with a reduced Atlantic influence (Acaso, 1983; Pedraza, 1994; Muñoz et al., 1995; Muñoz-Salinas et al., 2013). The CvT peaty system had a set of natural water ponds of phreatic origin with perennial freshwater. The bog is located inside a semi-endorheic basin with seasonal stream flow linked to the precipitation-evapotranspiration balance. It can be supposed that relatively thick alluvial sand and gravel overpressured aquifers provide a perennial supply

to the CvT stream, as occurred in similar bogs from the region (Carrasco et al., 2018) when no surficial waters flow through the flat plain or there is snow cover in the winter season.

#### 4.2. Borehole

The combined interpretation of the DPSH test and the Borehole S1 has provided valuable information about the stratigraphy of the CvT subsoil (Fig. 4A). The DPSH test diagram shows two zones of dynamic cone resistance (Qd): one zone from the surface up to 1040 cm of depth with a variable pattern and another zone where the strength progressively increases up to 1280 cm (Fig. 4C). The zone with variable pattern suggests a highly heterogeneous infill up to 1040 cm. From there the progressive increase of penetration resistance suggests a more homogeneous material.

The S1 borehole provided 11 sediment cores (Fig. 4B) that can be grouped into six sedimentary sequences (SD) based on stratigraphical criteria (from bottom to top; Fig. 4C):

-The SD0 occupies the 1280–1000 cm interval and is mostly identified based on the sediment strength recorded by the dynamic sounding device. No cores are available between 1280 and 1040 cm because its low fine grain-size content and its cohesionless nature. Considering the geological context, depth and penetration resistance, this could correspond to a morainic/till deposits. Only a sample between 1040 and 1000 cm is available and consists of oxidized green-bluish arkose sands (quartz and feldspars grains) that can be attributed to a rubefacted till.

-The SD1 is assigned to the interval 1000–875 cm. This is a finning-upward sequence, starting at the bottom with fine-to-medium grain-size sands and brownish silt mixed with fine sands at the top of the sequence, where organic brownish silt is found and interpreted as buried peat. This type of sedimentary facies evolution is linked to an alluvial plain going

from channel facies to flooding distal facies.

-The SD2 is assigned to the interval 875–615 cm. A 75 cm-thick interval without core is related to the very coarse grain-size texture of the sediments (mostly gravels). The rest is a finning-upward sequence starting with a mixture of brown silts and gravels followed by a mixture of green-brownish silts and coarse-to-fine sands, and finishing with a brown silts and medium-to-very fine sands mixture. The bottom of the sequence is interpreted as a channel lag deposit, while the upper part is associated with a more distal channel facies.

-The SD3 is assigned to the interval 615–315 cm. This sequence consists of an alternation of several finning- and coarsening-upwards cycles including microgravels, coarse-to-very fine sands, silts and clays. Coarsening-upward sedimentary cycles are interpreted, in the El Cervuno Meadows setting, as overbank deposits yielded by flooding and/or crevasse-splay.

-The SD4 is assigned to the interval 315–30 cm. This sequence consists of an alternation of several finning-upwards sequences starting at the base with non-rounded and rounded polymorphic gravels and/or coarse-to-fine grain sands mixed with silts. These sedimentary assemblages could be related to distal channel facies.

-The sequence SD5 corresponds to the interval 0–30 cm and consists of a pedogenic sequence with recognizable A-C edaphic horizons with sandy clay, gravels and roots.

#### 4.3. Geophysical interpretation

Due to the greater sensitivity, resolution and coverage achieved with resistivity methods (i.e., ERT and VES), electrical resistivity has proven to be the most informative physical parameter to interpret the complex subsurface geology of the CvT area. The analysis of the continuity and geometry of the resistivity gradients, as well as the lateral and vertical

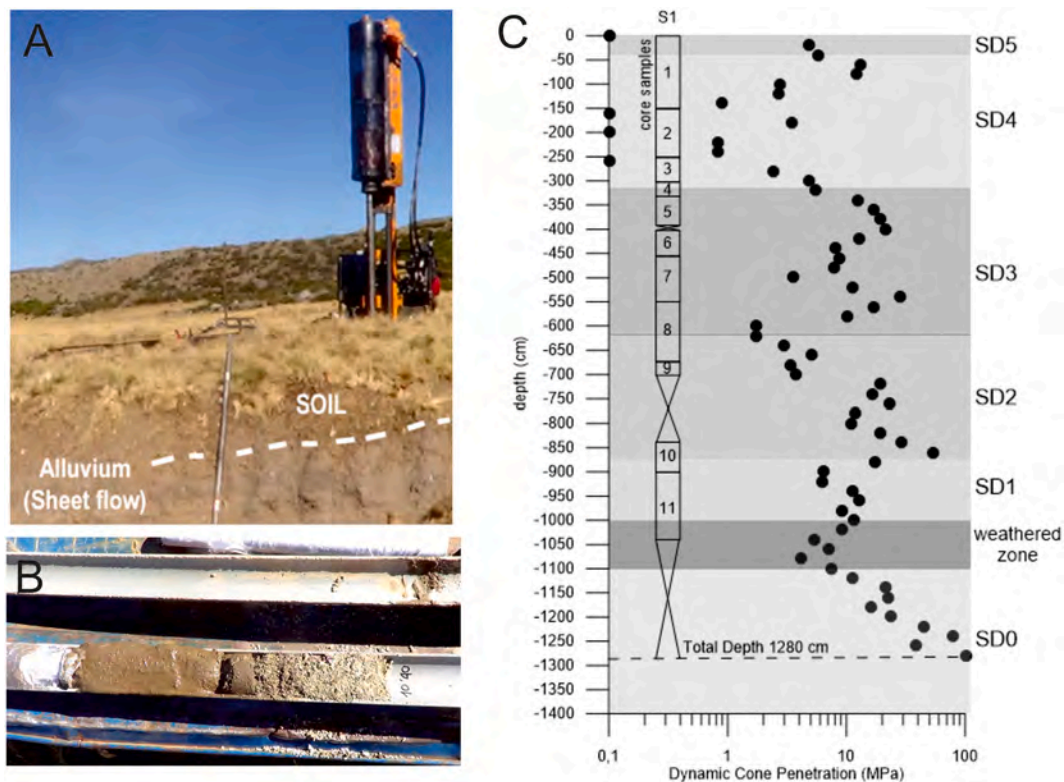


Fig. 4. Borehole. See location in Fig. 2A. A) Penetration sounding (DPSH) across the superficial soil and laminated fine grained sheet flow deposits (steel bar = 1 m-long). B) Core ending sample at 10.4 m of depth from borehole S1. Grain-size differences are visible from texture of the core. Bottom of the sample: medium sands from a supraglacial till (to the right) and brownish silts from colluvium/alluvium (to the left). C) DPSH Dynamic cone penetration resistance diagram from the DPSH test (black dots). Borehole S1 showing the core sampling intervals for 11 samples. SD5 to SD1 subdivisions of Unit 1 (Table 1) and SD0 correlates with Unit 3. Unit in between (U2) is not present in this borehole sounding.



distribution of relative maxima and minima, allows us to interpret distinct geo-resistive units. This initial interpretation based on resistivity is further integrated with the seismic interpretation (i.e., ST and ReMi) and MRS to get integrated geophysical units (see U in Table 1).

In the CVT case study, seismic methods have proven to be complementary techniques because they only enable us to identify the first order geophysical units. This is because of the lower resolution of the seismic deployment and the lack of significant velocity gradients in the trough infill, which prevents us from distinguishing second order geophysical units (see SU in Table 1). Similarly, the MRS was also a complementary technique providing information about the water content, permeability, and insights about the basement depth in the south-east of the trough (MRS in Fig. 2A). The 1D-model derived from the MRS inversion has numerical coherence up to 90 m of depth and shows that water is present at all investigation layers (Fig. 5B). Assuming the aquifer exists in the sedimentary fine-to-coarse grain-sized deposits lying over a low-permeable hard rock, the MRS interpretation is not conclusive. A possible interpretation for this would be that there is a weathered basement at approximately at 35 m where there is a significant decrease in permeability (i.e., low-permeable granite; Fig. 5D). This interpretation roughly agrees with VES and ERT (Figs. 6 and 7B) because there is sedimentary infill of at least 45 m of depth. An alternative interpretation for the decrease in permeability at 35 m of depth could also be related to an increase in fine grain-size sediments within the trough infill. Independently, the basement was also inferred in two VES in the northern closure of the CvT, but in this case, the basement is at shallower depths (~ 10 m) and there are two zones: a high-resistive zone (>8000 Ω·m) that could correspond to basement or morainic deposits, and a low-resistive zone (<2000 Ω·m) corresponding to weathered basement (see VES-1 and VES-2 in Fig. 6). In this place, this is coherent with the proximity of the granitic outcrops forming an elevation in the NW of the CvT close to the VES-1 and VES-2 (Figs. 2A and 3A). In sum, the limited information about the basement makes it harder to carry out reasonable reconstructions of the basal geometry of the sedimentary infill (c.f., Carrasco et al., 2018). However, both MRS and VES suggest that the sedimentary thickness is higher to the south than to the north of the CvT (Figs. 5 and 6). An additional insight provided by the MRS model is that the broad range of decay time (T2\*: 50–1000 ms) attests the presence of variable grain-sizes (i.e., from clays to gravels; Fig. 5C). This is confirmed by the borehole data and suggests a multilayered aquifer with variable amount of water from level to level.




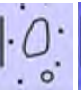
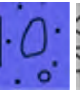

The resulting geophysical information is intended to enable a better understanding of the 3D distribution of the different geophysical bodies or units, but they need finally be constrained and validated by the geomorphological information and borehole data. Based on the combined interpretation of geophysical methods with the geomorphological and borehole data, the sedimentary infill of the CvT can be classified into three main geophysical units (U1, U2 and U3 in Table 1).

#### 4.3.1. Unit 1

Unit 1 (U1) consists of the shallower geophysical layer covering the interior of the CvT and overlain by units 2 (U2) and 3 (U3) (Fig. 7). U1 unconformably onlaps the boundaries of the trough, mostly consisting of U3 morainic deposits (Pinar, Cabeza-Nevada and Gredos glacial systems), and in the NW region the granitic basement hill (Fig. 3A). It is characterized by a broad range of resistivity values from 2000 to 10,000 Ω·m (locally >10,000 Ω·m; Table 1). The base of this Unit is marked by a steep, highly continuous, and sinuous sub-horizontal resistivity gradient (Fig. 7). This steep gradient suggests a clear contact of U1 lying unconformably on U2 and U3. The gradient is negative in the transition to U2 (i.e., from high to low resistivity) and positive towards U3 (i.e., from low to high resistivity). In most of the CvT the thickness of the U1 averages between 4 and 6 m (locally up to 15 m) (e.g., see 280–300 m of distance in ERT2/3, and ERT4 in Fig. 7; Figs. 6 and 8B).

The average resistivity of U1 shows a northward decrease with a predominance of higher values in the south (>5000 Ω·m) and lower

**Table 1**  
Classification and characterization of the Geophysical Units (U) and Sub-units (SU). Physical parameters, materials and associated processes.

| U  | SU    | H (m)    | legend  | ERT (Ω·m)       | VES (Ω·m)  | Vp (m/s)  | Vs (m/s) | Poisson ratio | MRS Water content (%) | MRS Permeability (m/day) | Sediment grain-size              | Processes                  | Direct observations (Borehole S1) |
|----|-------|----------|---|-----------------|------------|-----------|----------|---------------|-----------------------|--------------------------|----------------------------------|----------------------------|-----------------------------------|
| U1 | SU1.1 | 4–6 (15) |   | 2000–5000       | 600–13,000 | 300–1500  | 98–326   | 0.44–0.47     | 0–25                  | 1–58                     | Fine-intermediate                | Soil, peat, alluvial plain | Post-glacial SD5 to SD4           |
|    | SU1.2 |          |  | 5000–10,000     |            |           |          |               |                       |                          | Intermediate-coarse              | Alluvial fan-channel       | Post-glacial SD3 to SD1           |
|    | SU1.3 |          |  | >10,000         |            |           |          |               |                       |                          | Coarse (gravels)                 | Alluvial fan-channel       |                                   |
| U2 | SU2.1 | >20      |  | 500–1500        | 700–1300   | 1500–2500 | 300–800  | 0.40–0.48     | 4–6                   | 27–30                    | Fine-intermediate                | Glaciogenic (kame)         | Glacial (not observed or exposed) |
|    | SU2.2 |          |  | 1500–5000       |            |           |          |               |                       |                          | Intermediate-coarse              | Fluvioglacial (kame)       |                                   |
| U3 |       | >20      |  | >5000 (>20,000) | 4000–6500  | >2000     | >750     | 0.44          | 7–8                   | 5.4–8.5                  | Cobbles, boulders, coarse matrix | moraine                    | Glacial SDO                       |

ERT = Electrical Resistivity Tomography, VES = Vertical Electrical Sounding, MRS = Magnetic Resonance Sounding, Vp = P-wave velocity, Vs = S-wave velocity, H = Thickness, SD = Sedimentary sequence (Borehole S1).

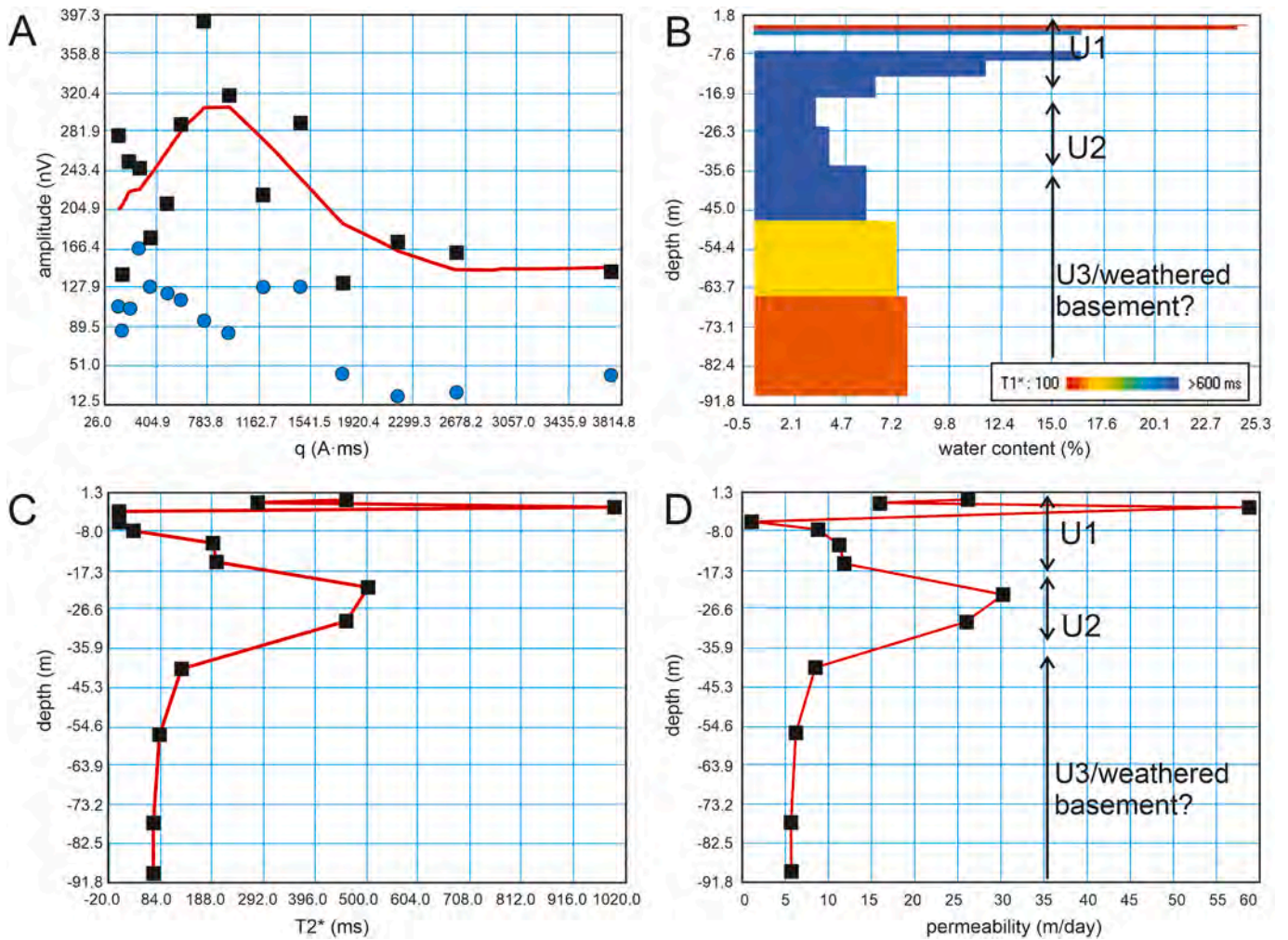


Fig. 5. Magnetic Resonance sounding (MRS) inversion results. Geophysical units (U) are drawn in B and D. A) Field data.  $q$  = electromagnetic pulse. Black squares show measured data. Blue circles show electromagnetic noise. Red line shows fitted inversion curve. B) Water content or saturated porosity (%). C) Decay time ( $T2^*$ ). D) Permeability. (For interpretation of the references to colour in this figure legend, the reader is referred to the web version of this article.)

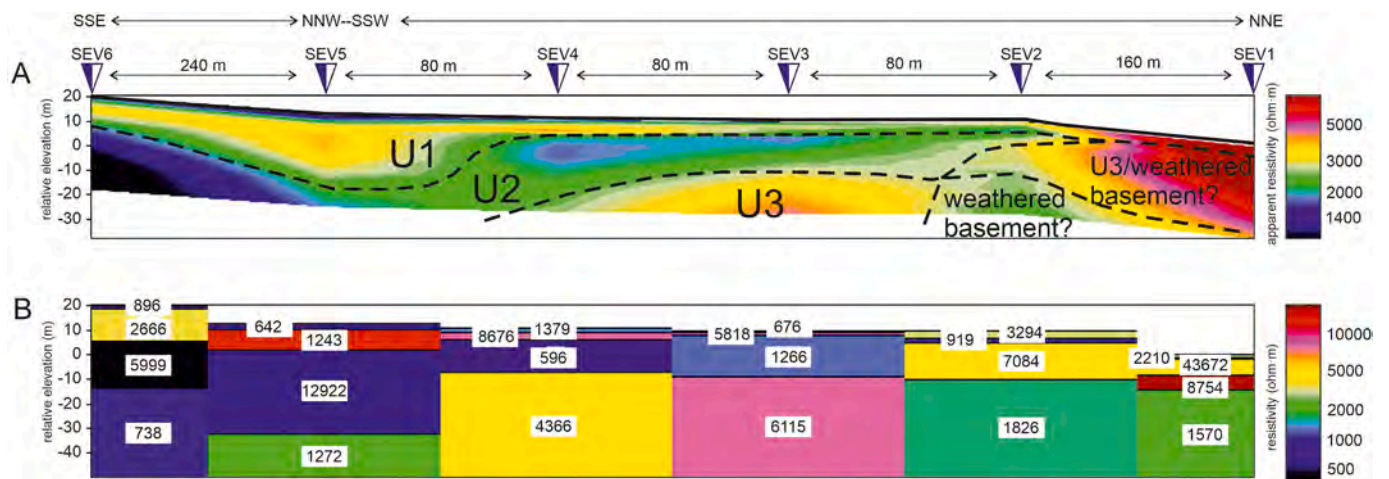
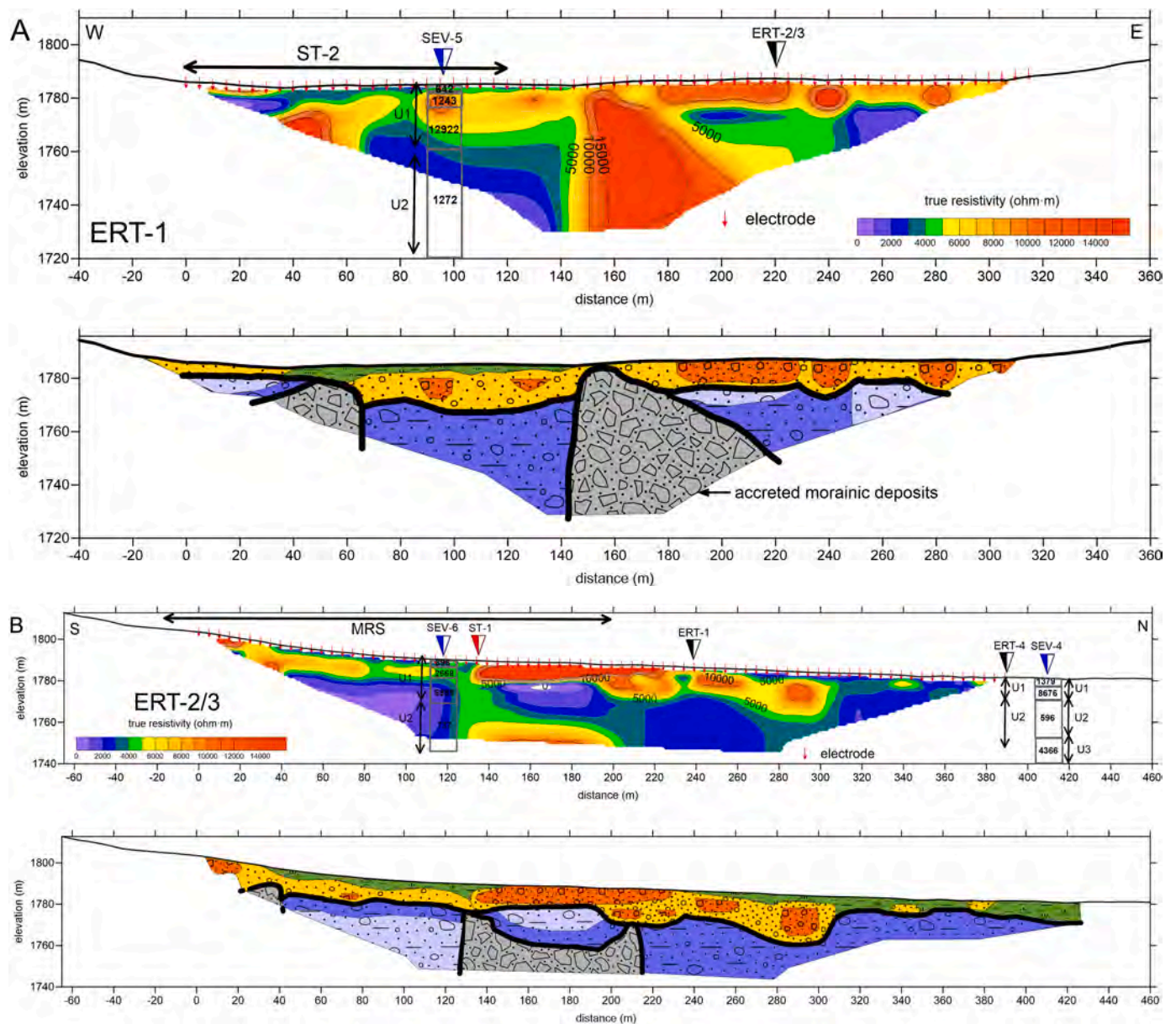


Fig. 6. 2D Vertical Electrical Sounding correlation with IPI2Win software (Bobachev et al., 2003). See location in Fig. 2A. A) Pseudo cross-section. U = Geophysical units. B) Resistivity cross-section.



**Fig. 7.** 2D Electrical Resistivity Tomography (ERT). See Location in Fig. 2A. Top: 2D resistivity model. Bottom: interpretation (see colour and pattern codes in Table 1). A) ERT-1. B) ERT-2/3. C) ERT-4.

values in the north ( $<5000 \Omega\cdot m$ ) (Figs. 6 and 7). This can be attributed to the predominance of coarser grain-sized sediments in the south related to the alluvial-fan system and finer grain-sized sediments in the north related to the alluvial plain and soils (Fig. 3A). The broad range and highly variable resistivity values of U1, irrespective of the inherent higher resolution of the ERT method at shallower levels, could be attributed to coarser grain-size heterogeneity. This feature was observed in the borehole data (Fig. 4) showing high layer alternation and frequent changes of grain-size facies ranging from fine to very coarse sediments that were sometimes poorly classified. This, as will be shown below, is a big difference with respect to U2 and U3, which seem to be more homogeneous (even assuming inherent lower resolution of the ERT at deeper levels). The broad ranges and lateral changes in resistivity can be attributed to lateral changes in facies within U1. Three sub-units were identified (SU1.1, SU1.2 and SU1.3 in Table 1; Fig. 7): SU1.1 shows lower resistivity values and is consistent with finer grain sediments like soil, peats and alluvial plain; SU1.2 shows intermediate resistivity values

consistent with medium-to-coarse sediments related to the alluvial fan system; and SU1.3 shows higher resistivities consistent with coarser sediments up to gravels related to the alluvial fan system. This alluvial fan system outcrops south of the CvT and was observed during field work and was quite well-mapped by photointerpretation (vegetation + topographic expression: Fig. 3A). This active fan system is formed by a current stream flowing northward throughout the center and southern sectors of the basin, whereas it is buried laterally and northwards beneath the lower resistive material of SU 1.1 (Fig. 7B).

Our seismic models allow us to interpret the contact of U1 with the U2 and U3 by means of a continuous sub-horizontal velocity gradient (Fig. 8). However, unlike the resistivity, the seismic gradients are smoother and thus less resolutive for mapping the contacts among the geophysical units. U1 also shows a broad range of P-velocities and S-velocities between 300 and 1500 m/s, and between 98 and 326 m/s respectively (Table 1; App. E). This is coherent with the observations using electrical methods and agrees with the significant heterogeneity in

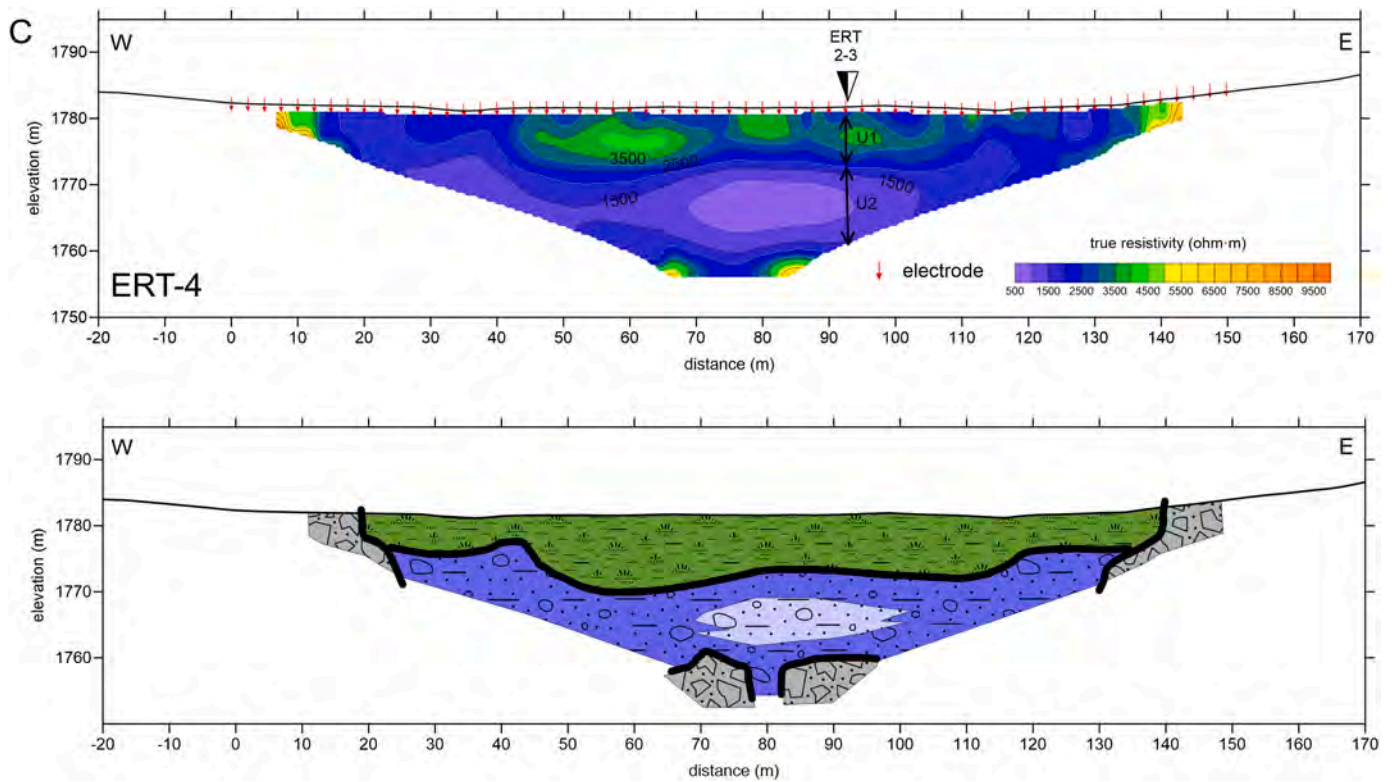


Fig. 7. (continued).

grain-size and lithology. S-wave velocities are significantly low and thus the Poisson ratio varies between 0.44 and 0.48, suggesting unconsolidated material. The lower velocity values are coherent with relatively low overconsolidation ratios (i.e., the predominance of soft sediments related to peat, alluvial plain and colluvium), and the higher relative values also with higher consolidated materials. Frequent lateral velocity variations suggest lateral change in facies between soils, alluvial plain and alluvial-fan deposits (Table 1; Fig. 8A). In the case of the ReMi, the 1D S-velocity models have shown distinct results for U1 (Fig. 8; App. E). This is likely controlled by the location of seismic deployment and the heterogeneous lithology in the CvT. The ReMi-1 has one seismic layer of relative higher average S-velocity of 290 m/s because it is closer to the alluvial-fan system, and the ReMi-2 has two seismic layers of 98–138 m/s and 239–326 m/s that could be related to alluvial plain and alluvial-fan settings, respectively.

The 1D MRS model shows that U1 has a variable water content and permeability (Table 1; Fig. 5). This is well correlated with the highly heterogeneous nature and grain-size of sediments in the CvT. The water content varies between 12% and 25%, and permeability between 1 m/day and 58 m/day. There is a noticeable lack of water content between 3.3 m and 7.6 m of depth (Fig. 5B) that can be attributed to the presence of a clay rich layer (i.e., since the only water detected by MRS is “free water” and the water stored in clay has a very short decay time, it is not normally detected because of instrumental limitations). This lithology should be related to the sedimentary sequence SD3 interpreted as overbank deposits having significant content of fine sediments. In addition, it is also relevant that U1 also shows a noticeable layer of high permeability (58.01 m/day) around 4 m of depth (Fig. 5D) that could be related with the sedimentary sequence SD2 with high gravel content (Fig. 4).

#### 4.3.2. Unit 2

U2 is always below a steep, highly continuous, and sinuous sub-horizontal resistivity gradient that marks an unconformable contact with U1 (Fig. 7). Laterally U2 is discontinuous and bounded by steep sub-vertical gradients that marks the contact (mostly onlap) with U3 (morainic materials). Average U2 resistivity values mark a relative minimum compared with U1 and U3, and are more homogeneous than U1. U2 shows a narrower range between 500 and 1500  $\Omega$ -m, though locally it can reach 5000  $\Omega$ -m (Table 1; Fig. 7). Resistivity values are consistent with fine-to-medium grain-size materials related to glaciogenic deposits (<1500  $\Omega$ -m; SU2.1 in Table 1), and locally coarser sediments related to fluvio-glacial deposits (<5000  $\Omega$ -m; SU2.2 in Table 1). Both deposits are coherent with the alternating lithology of sedimentary sequences SD3, SD2 and SD1 described in the borehole (Fig. 4).

U2 shows P-velocities ranging between 1500 and 2500 m/s and S-velocities ranging between 300 and 800 m/s (Table 1; Fig. 8; App. E). These relative higher values of velocity suggest high stiffness materials than U1, which is coherent with higher lithostatic compaction at deeper levels. However, the Poisson ratio is still >0.4 suggesting low consolidation. It is noteworthy that there are no evident velocity gradients between U2 and U3, in contrast to the electrical resistivity models (Fig. 8). This could be related to the experimental setup limitations of the ST (i.e., it would be needed shorter intervals for shot and receivers) in that it is not efficient enough to detect vertical contacts, and also because it is likely that both units have similar velocity ranges. This last issue can be attested by the similar ranges of Poisson ratio between both units (Table 1).

The 1D MRS model shows a water content between 4% and 6% and permeability values between 27 m/day and 30 m/day (Table 1; Fig. 5). This combined decrease in water content and permeability relative to U1 could be interpreted as a relative increase in fine-grain materials in U2.

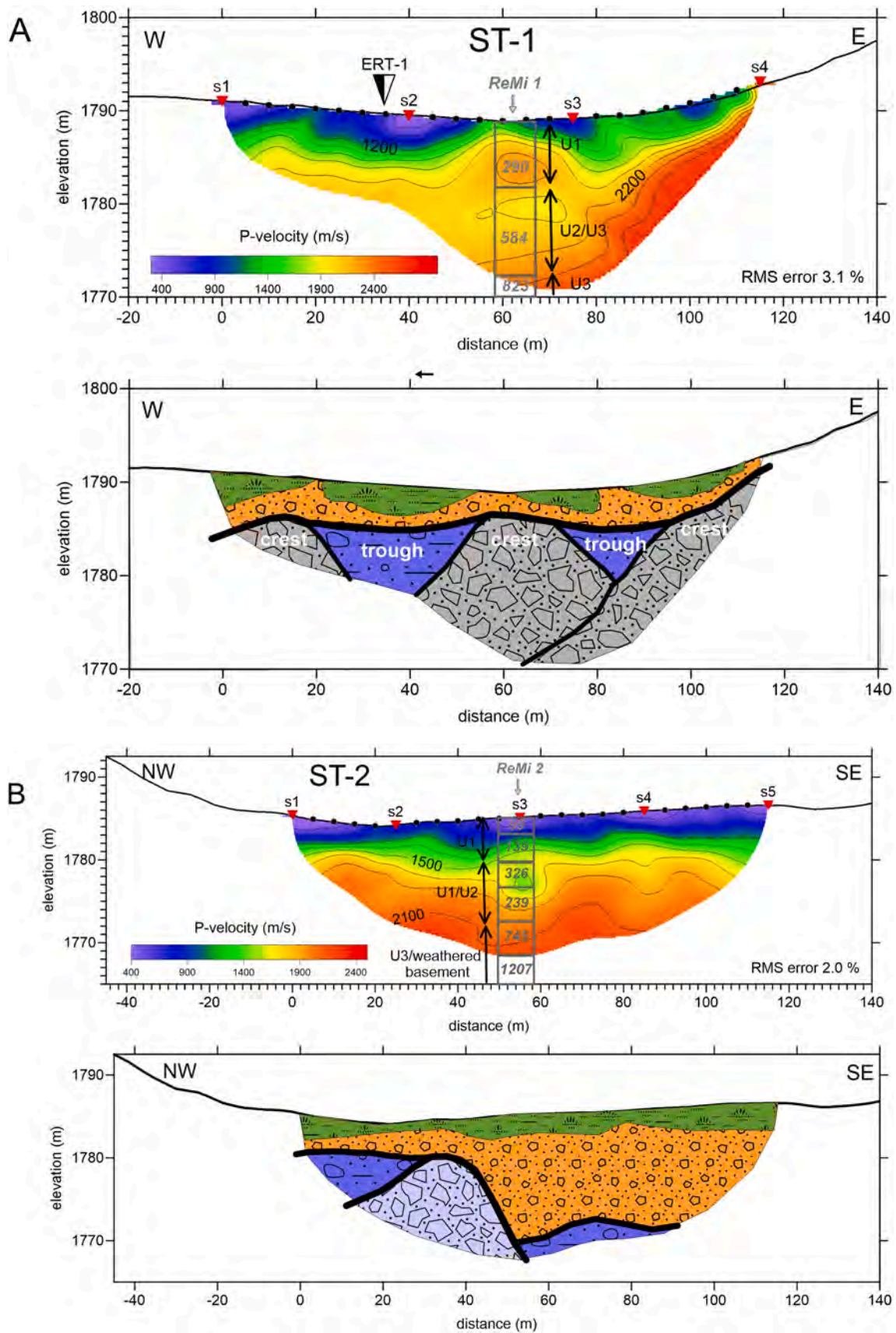


Fig. 8. Surface Seismic Tomography and ReMi. See location in Fig. 2A. See legend in Table 1. Top: 2D Model of P-wave velocity and 1D-model from ReMi in gray (Vs in m/s; App. E). Bottom: Interpretation of geophysical units. A) ST-1 and ReMi-1. B) ST-2 and ReMi-2.

The thickness of this unit is variable, but it is at least 20 m derived from the electrical and seismic methods (Figs. 6, 7 and 8) and approximately 20–25 m as inferred from the MRS (Fig. 5).

#### 4.3.3. Unit 3

U3 shows average resistivity values  $>5000 \Omega\text{-m}$ , reaching locally of  $20,000 \Omega\text{-m}$  (Table 1; Fig. 7). This unit is characterized by resistivity maxima limited by steep sub-horizontal gradients which mostly mark the contact with U1 and sub-vertical gradients which mark the contact with U2. This unit is laterally discontinuous and is replaced by U1 at shallower levels and by the U2 at deeper levels.

U3 shows average P-wave velocities  $>2000 \text{ m/s}$  and S-wave velocities  $>750 \text{ m/s}$  (Table 1; Fig. 8; App. E). Although there is an overlap in the velocity range (see also this overlap in the Poisson ratio in Table 1), in general, the average velocities are higher in U3 than U2. This fact together with the absence of clear sub-vertical velocity gradients makes difficult to map the contact between U2 and U3 in the seismic models. However, ERT and P-wave seismic models reveal a remarkable undulating geometry of a sub-horizontal gradient which marks the top contact with U1, providing insight to map this contact (Figs. 7 and 8). The alternation of troughs and crests emulates a paleorelief surface and is a good guide to locate below the U3 (crest) and U2 (trough) units beneath. This is useful to interpret the P-wave seismic model where there is no clear evidence of the contact between U2 and U3 (Fig. 8A).

The 1D MRS model shows a change in the water content and permeability at around 35 m of depth (Fig. 5). At deeper levels, the water content is stable averaging 7–8% and permeability significantly decreases, becoming stable around 6.4 m/day up to 90 m of depth. This change in both parameters at around 35 m of depth could be attributed to the contact between U2 and U3, but also to the top of the weathered basement. Both hypotheses are reasonable because of the significant water content and the low permeability. However, looking to similar previous experiences in Navamuño depression (ICS), Carrasco et al. (2018) documented  $<1\%$  of water content for the grus or weathered granites. Since Gredos and Navamuño have similar basement lithology, the MRS would not reach the bottom of the CvT paleovalley. Although the base of this unit was not identified because of experimental setup limitations, the minimum thickness is at least 20 m (Figs. 6, 7 and 8). However, if we consider the MRS data this thickness could reach 45 m (Fig. 5).

Unfortunately, the maximum depth reached by the borehole did not encounter U2 (Fig. 4). The outcrops in the CvT borders, however, show that moraines are diamictons mostly composed of angular cobbles and boulders of granitic lithology embedded in a scant coarse-grained matrix formed by weathering products (Fig. 3; Rubio et al., 1992; Carrasco et al., 2020).

The geometry and location of U3 in the context of the trough infill suggests that this unit is an analogue of continuous morainic arcs with well-defined crest-shaped ridges mapped in the surroundings of the CvT (Fig. 3). These moraines correspond to the mid-lateral moraines of the Gredos and El Pinar paleoglaciers and the latero-frontal moraines of Cabeza-Nevada paleoglacier. Carrasco et al. (2020) have assigned all these moraines to the morpho-stratigraphic formations called “Peripheral Deposit” and “Principal Moraine” which indicate, respectively, the evolutionary stages of the Glacial Maximum and the Maximum Stabilization of glaciers in these mountains (Pedraza et al., 2013; Carrasco et al., 2015b; Oliva et al., 2019). In the case of the CvT, moraines (U3) and adjacent kames (U2) are buried or partially buried by the post-glacial deposits of U1. Locally, U3 shows a surprisingly large resistivity anomaly that could be reasonably interpreted as a vertical and lateral accretion or accumulation of moraines (see accreted morainic deposits in Fig. 7A).

## 5. Discussion

### 5.1. Applicability of geophysical methods

The combined interpretation of diverse geophysical methods and geological information (geomorphology and borehole) allowed us to distinguish and locate the buried morainic and kame deposits beneath the postglacial Holocene infill of the CvT. Regarding the geophysical information, resistivity-based techniques have proven to be the most valuable prospecting methods. The morainic bodies show an outstanding geophysical signature having extremely high resistivities which are well-identified with electrical techniques (ERT and VES). However, the higher vertical and lateral resolution provided by 2D tomographic electrical techniques as ERT have shown to be much more efficient and informative when mapping the steep bounding-gradients between kame and morainic deposits, and lateral changes in facies in the postglacial Holocene infill allowing us to distinguish in more detail distinct geophysical sub-units. Therefore, ERT was used as the principal method to interpret distinct geo-resistive units. Unfortunately, during the geophysical acquisition survey, only four ERT profiles were recorded, providing a limited data coverage and depth range. Under these circumstances, VES was found to be a useful complement because, when calibrated with the ERT results, it allowed us to extend the subsoil interpretation over larger areas of the CvT. However, VES only provides the identification and correlation of the first order geophysical units. Therefore, in order to get a complete data coverage with which to study the subsoil of the CvT, it would be necessary to carry out a more extensive data acquisition by means of across- and along-strike ERT profiles (i.e., regular acquisition grid). The profile interval should be between 25 and 50 m to achieve a reasonable lateral correlation of the geophysical units and sub-units from a 2D inversion. Another option would be to carry out a 3D ERT acquisition and then a 3D inversion. Additionally, increasing the length of the profiles and the injected current would allow to study deeper targets and this way reach the basement. This procedure would provide an outstanding resolution; however, due to the significant extension of the survey area (about 32.5 ha), it would need major logistic and economic efforts.

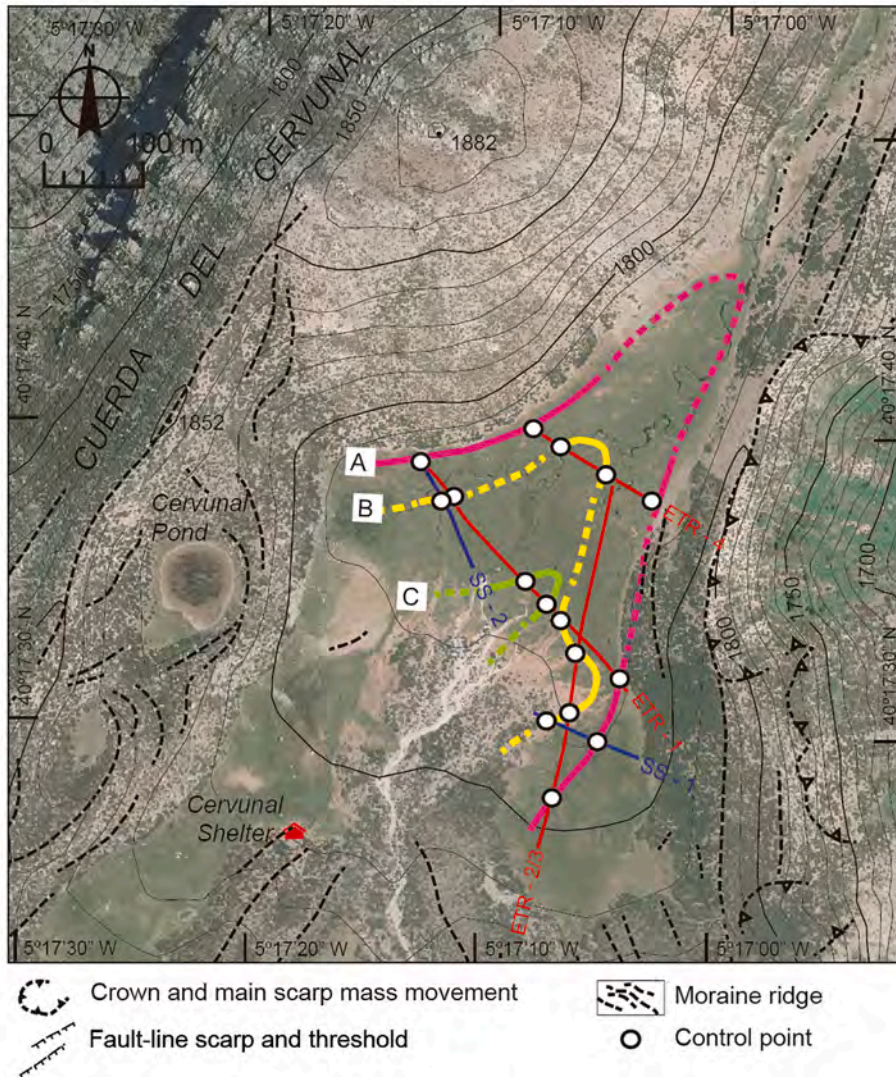
Seismic methods have been found to be less resolute than electrical ones and, consequently always provide complementary data. They only allow the identification and correlation of the first order geophysical units, and locally the sub-units in U1, but with significant uncertainty. The main limitation observed if seismic methods are applied in the study of the CvT is the lack of significant velocity gradients to properly map the lithological contacts in the subsoil. Both P-wave tomography and Refraction Microtremor methods allow us to better distinguish sub-horizontal contacts (i.e., between U1 and U2–U3), but they are strongly limited with sub-vertical contacts like the ones observed in the contact between kame and moraine deposits with resistivity-based methods. Indeed, even if we improve the seismic resolution by reducing shot and receiver intervals, the detection of sub-vertical contacts is always an inherent limitation for seismic methods (e.g., Reynolds, 2011). The best seismic contact identified was the base of U1 (post-glacial deposits). This velocity interface shows an undulating morphology with crests and troughs that was locally useful to infer the location of morainic (crest) and kame deposits (trough; Fig. 8A). In the case of the Refraction Microtremor method, the 1D S-velocity models show significant distinct results (ReMi 1 three layers and ReMi 2 six layers; App. E), likely as a result of the heterogeneous subsoil geology and the location of seismic deployment in the CvT setting. The ReMi-1 is closer to the alluvial-fan system and thus shows a higher average S-velocity for U1 than the ReMi-2 which is located in a dominant alluvial plain setting. Both ReMi models detect a seismic layer between 500 and 800 m/s that could be attributed to U2 and/or U3. The ReMi-2 has the deepest layer with a Vs of 1200 m/s that could suggest a more consolidated U3 (till) or a weathered basement (Fig. 8B). While these models were not very informative regarding the lateral subsoil geometry, they

proved useful in order to get an estimation of consolidation using the Poisson ratio and the increase in the investigation depth up to 30 m. For more insight on the subsoil geometry of the CvT, this method should be applied as a systematic acquisition procedure, varying the receiver position along the profile (e.g., Louie, 2001). This procedure makes it possible to obtain several 1D models that could be laterally correlated to build a S-wave pseudo-section with better lateral resolution that would be much more comparable to the P-wave tomography.

MRS has proven to be a good complementary method to estimate the water content and permeability of the sedimentary section. MRS results provided 1D model, but only representative for the southeast region of the CvT. The limitations of this method are the same as those of 1D models when lateral changes in the geometry of the geological units exists. However, the MRS has significant larger depth range than the rest of the applied geophysical methods and, therefore, it is a good complement. The acquisition of several MRS occupying regularly the CvT area would provide information to infer the thickness of the saturated aquifer and also to estimate the basement depth, contributing to perform reasonable reconstructions of the basal geometry of the sedimentary infill (c.f., Carrasco et al., 2018).

### 5.2. Reconstruction of the CvT glacial setting

The location of morainic (U3) and kame (U2) deposits allows to infer the geometry of the retreat of the paleoglacier system hosted in the CvT, which it is currently almost buried by postglacial deposits (U1). From the control points provided by the geophysical data and the combined interpretation with the geomorphological data, it is possible to reconstruct the map-view geometries of the morainic bodies in the CvT interior (Fig. 9). Taking the location of U3 as the main reference in the trough infill, the moraines defined by crest-shaped ridges can be continuously mapped applying reasonable geometries and analogies with the dynamics observed in glacial system retreats. At least three continuous arcuated ridges could be mapped in the center and northern region of the CvT (from older to more recent A, B and C; Fig. 9). However, drawing the continuity of those ridges towards the south and southwest of the CvT results problematic because of the lack of data. This fact yields strong uncertainty in the interpretation of ice flow during these evolutionary stages and consequently, the correlation of these morainic deposits (i.e., A, B and C) with the three paleoglaciers bounding the CvT (i.e., Gredos, El Pinar and Cabeza-Nevada; Fig. 3). An extended geophysical data coverage of the south and southwest of the CvT would be necessary to provide more control points which would contribute to map the morainic bodies in more detail, and thus, to assess



**Fig. 9.** Reconstruction of the glacial system retreat in the CvT. Background shows an orthophoto (Instituto Geográfico Nacional, [www.ign.es](http://www.ign.es)). Geophysical data location as in Fig. 2A. A, B and C labels show distinct interpreted crests of morainic arcs (continuous thick lines show well-constrained interpretation and dashed thick lines are inferred). According to the surface geomorphological indicators, these three morainic arcs represent sequences of retreat-stabilization and correspond to the Peripheral Deposits formation (see Fig. 3). Its development has been established between the Glacial Maximum and the beginning of the Deglaciation Stages (Pedraza et al., 2013) and whose chronologies are ~26 ka BP and ~ 19 ka BP, respectively (Palacios et al., 2011, 2012; Oliva et al., 2019).

the cross-relation with surrounding paleoglacier systems properly.

Although the assignment of the interpreted morainic arcs to one or another paleoglacier system remains unclear, significant insights on the formation of the CvT can be derived from this study. The results indicate a complex evolution for the CvT deposits, where erosive-sedimentary processes dominate, but also that structural factors should be considered. Considering the morphological and geophysical units present in CvT and the regional setting, at least five well-differentiated stages can be established to explain the occurrence of the trough infill:

- The first stage corresponds to the pre-glacial evolution, in which the paleovalleys of the Gredos and Pinar gorges were installed on NNE-SSW fractures. During this stage, it can be recognized how the interfluvium between both gorges presented a major discontinuity in the topography, forming a wide NE-SW topographic corridor that could connect both valleys (Fig. 1).
- The second stage corresponds to the evolution during the phases of glacial expansion, which include the Maximum Ice Extension (MIE), the subsequent sub-stages associated with this maximum, and a final sub-stage of limited retreat. These evolutionary phases are indicated by the peripheral deposits (PD formation; Pedraza et al., 2013), clearly identified along the limits of the CvT (Figs. 3 and 9), which were deposited between ~26–24 ka to ~20 ka BP (Oliva et al., 2019). At the onset of this evolutionary stage, the topographic corridor between the Gredos and Pinar gorges was a suitable area for the interconnection of the ice corresponding to both glaciers and that of Cabeza Nevada. In the immediate post-MIE stage, the buried moraine system detected in this investigation could be attributed to minor retreats during this stage (morainic arcs: A, B and C in Fig. 9). This suggests that the glaciers in this area presented a series of oscillations relatively close to their maximum extent with limited retreat and stabilizations generating minor moraine systems (PD-M).
- The third stage is clearly delimited by the border moraines, which mark the definitive obturation of the CvT, giving it a configuration similar to the current one with slight variations at the bottom due to the later sedimentary filling process. During this stage, spanning from ~20 ka to ~17 ka BP (Oliva et al., 2019), a readvance followed by a significant stabilization-time of the ice took place, building the major border moraines (PM formation; Pedraza et al., 2013).
- During the fourth stage, the position of the lateral moraines and morainic arcs of Gredos, Pinar and Cabeza Nevada paleoglaciers (Fig. 3; ID formation; Pedraza et al., 2013) suggests that the retreat of the local glacial system or deglaciation took place between ~17 and ~14 ka BP (Oliva et al., 2019).
- The fifth stage corresponds to the attenuated periglacial and post-glacial environments. These were characterized by the development of alluvial fans, alluvial plains, and marshy areas with seasonal flooding, and at some points accompanied by slope deposits, which contributed to the final sedimentary infill of the CvT.

## 6. Conclusions

A set of 1D and 2D near-surface geophysical methods, including electrical (VES and ERT), seismic (ST and ReMi) and magnetic resonance sounding (MRS) techniques, supported by geomorphological and borehole data, were used in the CvT to test their applicability and to provide

better insight on the infill geometry, as well as the water content and permeability.

Due to the greater sensitivity and coverage of the resistivity methods (ERT and VES), electrical resistivity has proven to be the most informative physical parameter to interpret the complex subsurface geology of the CvT area. The 2D ERT method was found to be the most resolute and efficient method responding to the heterogeneous nature and complex geometry infill. 2D ST showed significant limitations because there are no significant velocity gradients to properly map the lithological contacts in the CvT subsoil. 1D models derived from VES, ReMi and MRS methods have shown reasonable vertical resolution but limited lateral resolution, preventing a detailed subsoil characterization. However, they were useful to constrain 2D methods, extending data coverage and increasing the investigation depth.

The infill of the CvT has been classified into three geophysical units (U) accompanied by their geological interpretation. From top to bottom these are: U1 is interpreted as the postglacial sedimentary sequence (mostly Holocene), and includes alluvial-plain and alluvial-fan deposits; and U2 and U3 are interpreted as glacial sequences including kame deposits (U2) and moraines (U3). The basement of the trough was locally inferred as weathered bedrock but because of instrumental setup limitations, there is scarce information to carry out reasonable reconstructions of the basal geometry of the sedimentary infill. Greater resolution provided by the ERT allowed us to interpret distinct geophysical sub-units (SU). In the postglacial unit (U1), SU1.1 corresponds with soil and alluvial plain (fine sediments), SU1.2 consists of alluvial fan (intermediate-fine sediments) and SU1.3 is related to alluvial fan (coarse sediments, gravels). In the glacial unit U2 (kame), SU2.1 corresponds with glaciogenic deposits (fine-intermediate sediments) and SU2.2 is attributed to fluvio-glacial deposits (intermediate-coarse).

The subsoil information provided by the combined interpretation of geophysical, geomorphology and borehole data allowed us to reconstruct the map-view geometries of a part of the morainic bodies in the CvT. These suggest a complex evolution, where erosive-sedimentary processes dominate, but also that structural factors should be considered.

## Declaration of Competing Interest

There is no any expected conflict of interest.

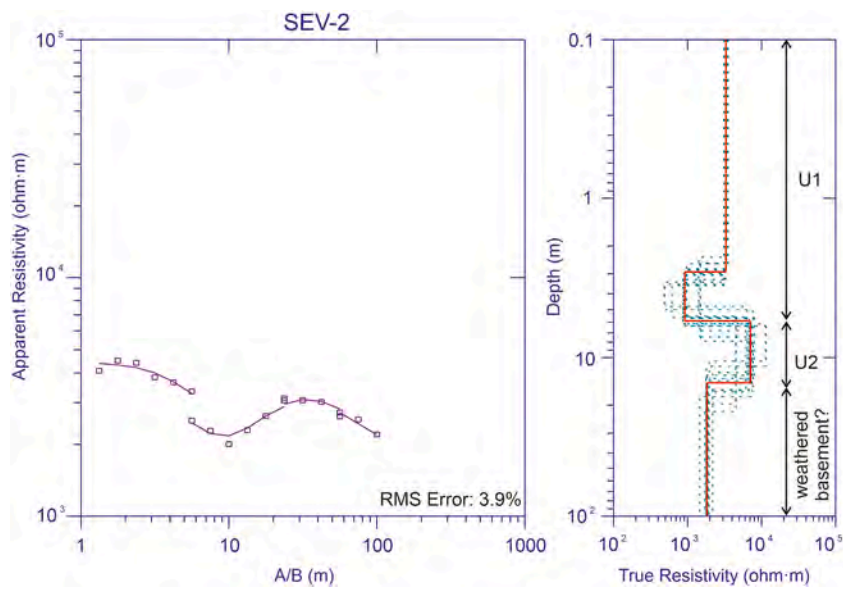
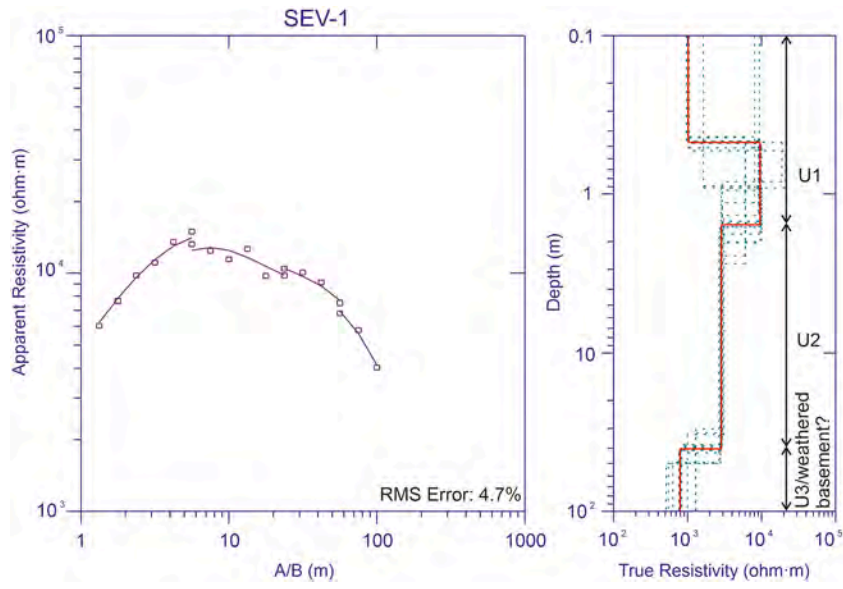
## Acknowledgements

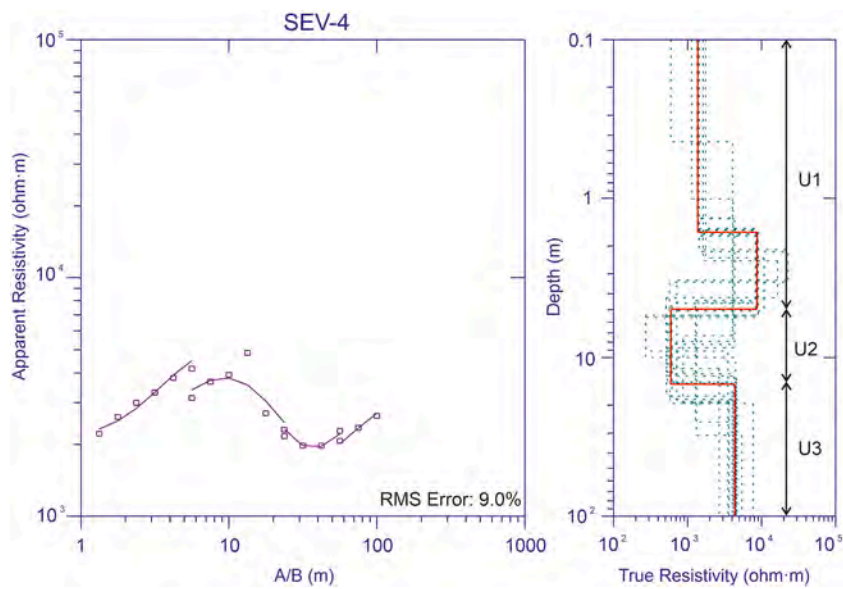
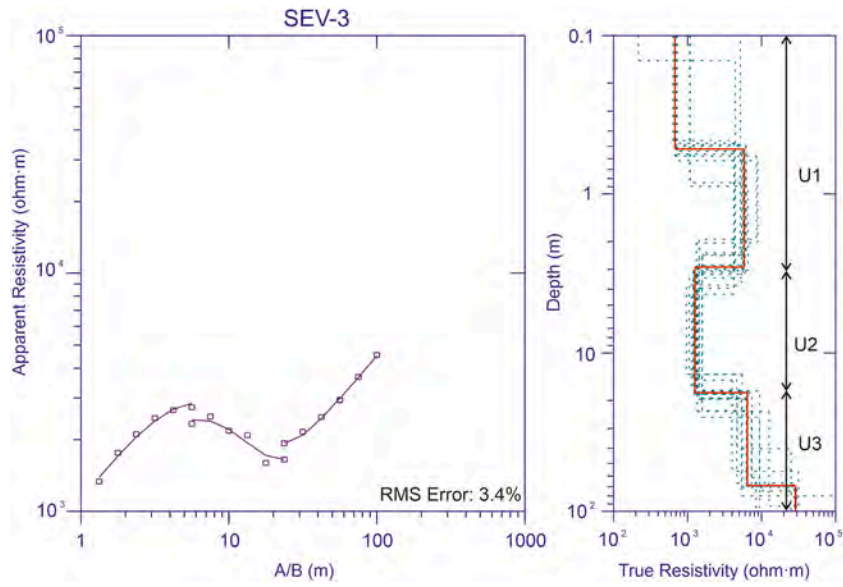
This work was mainly supported by the Spanish Ministry of Science and Innovation (Spanish initials: MINECO; project CGL2016-78380-P) and UCLM Research Groups (Project 2020-GRIN-28992). The authors acknowledge the help received from the Sierra de Gredos Regional Park and the Consejería de Medio Ambiente of the Junta de Castilla y León (JCyL). Additional support comes from the Program I+D CARESOIL (S2018/EMT-4317) of the Comunidad Autónoma of Madrid. Most data were processed under software academic licenses for Universidad Complutense of Madrid (Rayfract, SeisOpt, Res2Dinv, Golden Software, Global Mapper, Oasis Montaj). We would like to thank to editor, to Sebastian Uhlemann and to an anonymous reviewer for the valuable revision and suggestions to improve the quality of the paper.

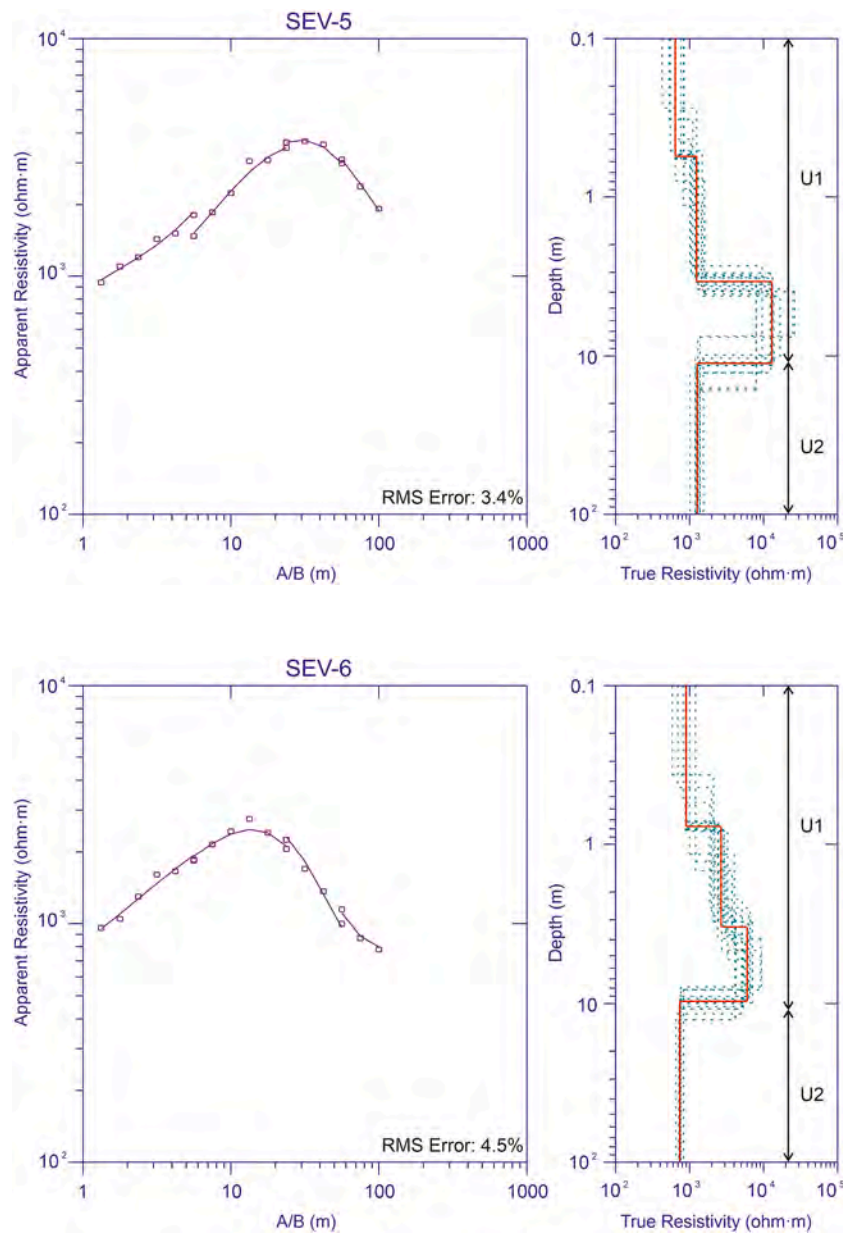
## Appendix A

Graphical results of the Vertical Electrical Soundings (VES). Left) Field measurements (squares). Repeated measures show MN spacing 0.5 m and 2 m. Adjusted dispersion curve (purple line). Right) 1D resistivity model (best model in red) and equivalent models in green dashed lines. Labels U1, U2 and U3 show the geophysical units.



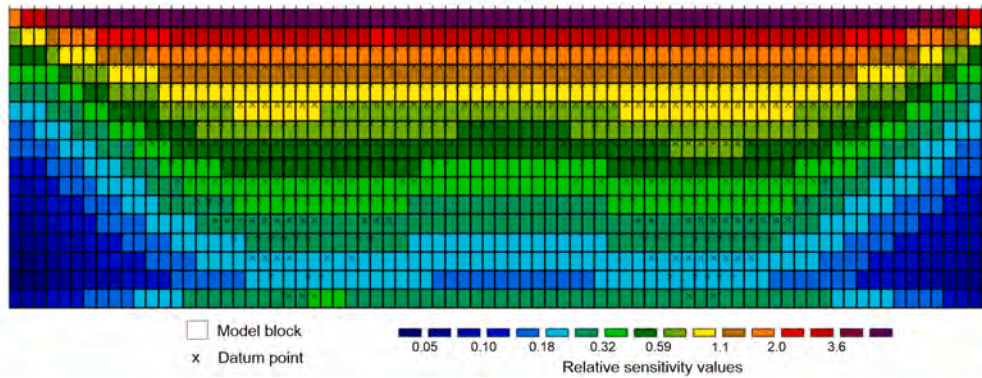
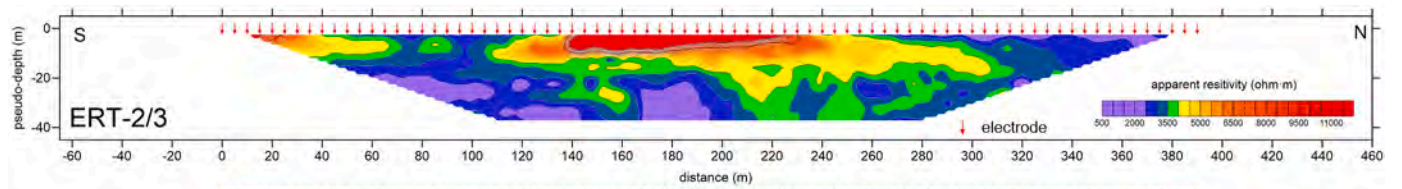
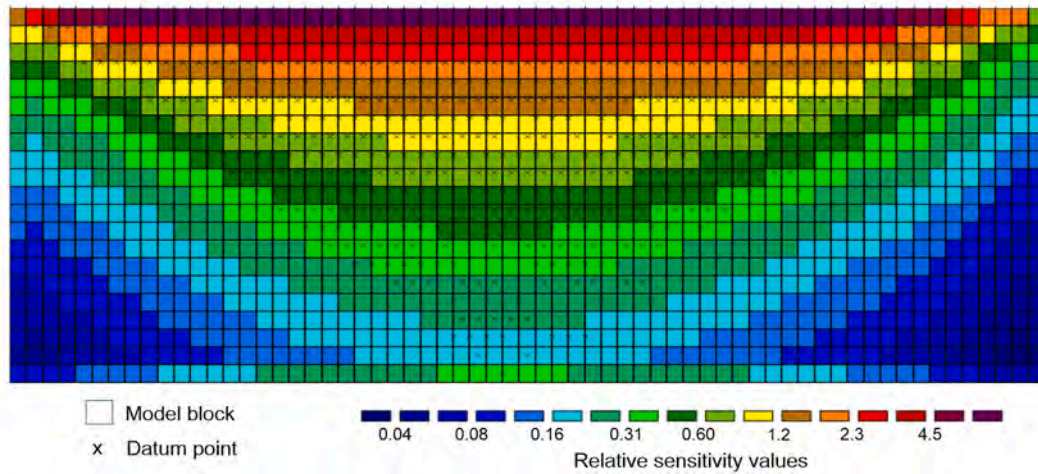
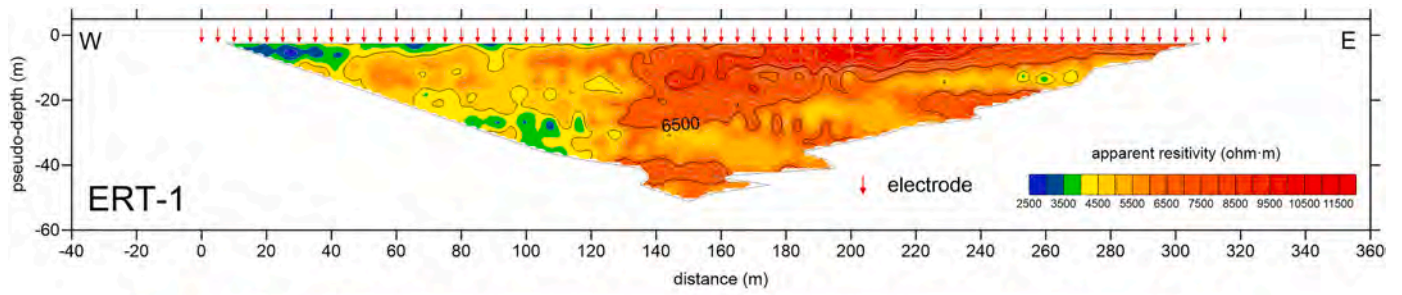


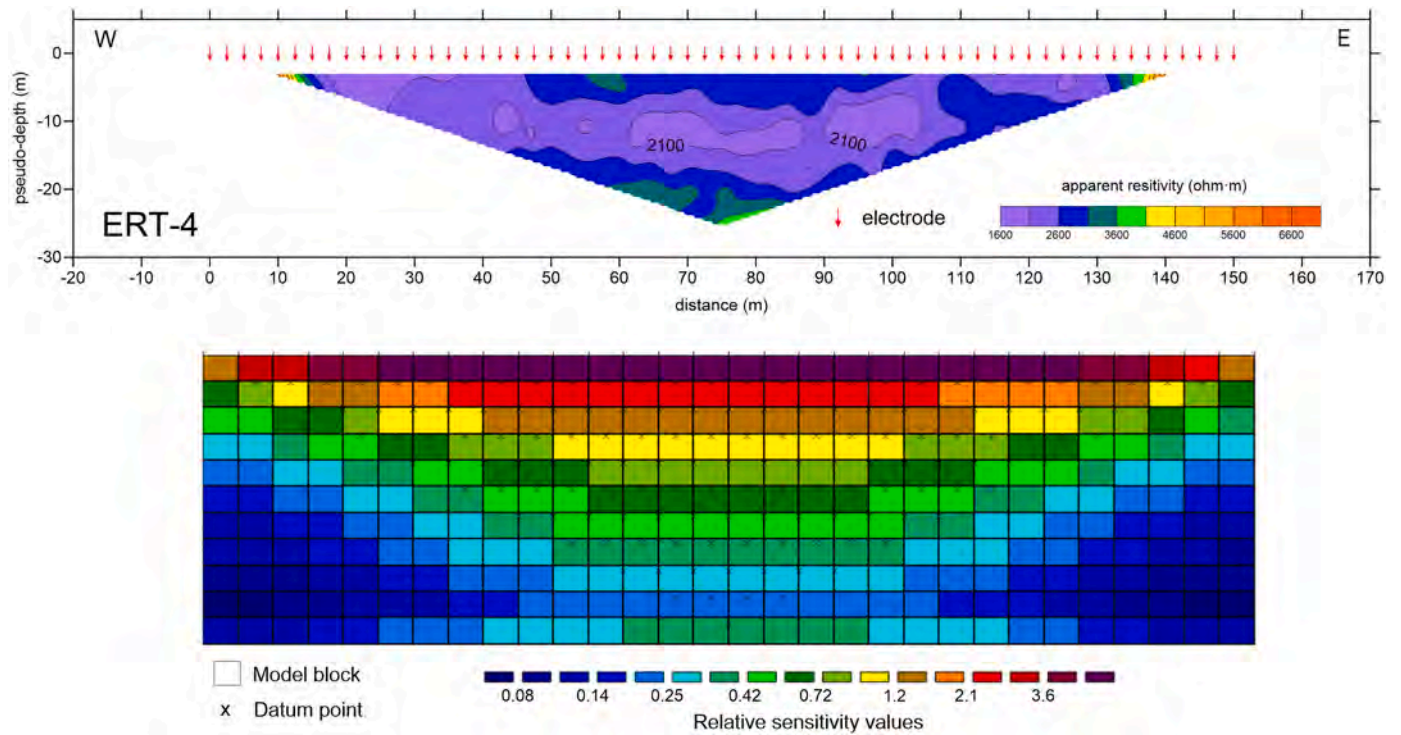




## Appendix B

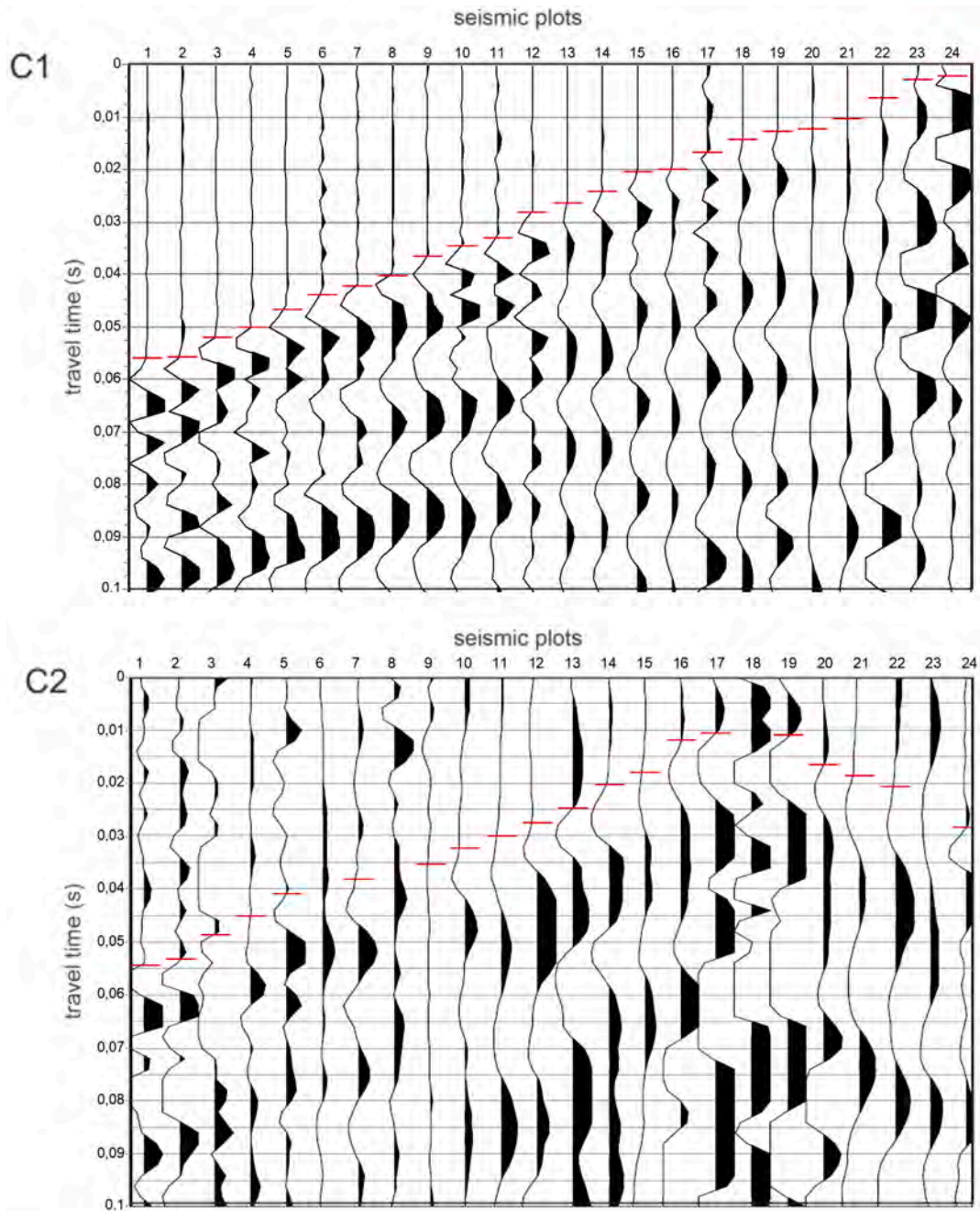
ERT data. See location in Fig. 2A. Top: ERT Pseudo-section (apparent resistivity vs. pseudo-depth). Bottom: Quantitative sensitivity analysis (Loke et al., 2013 and references therein). B1) ERT-1. Model layers = 21. Model blocks = 1323. Datum points = 544. Electrodes = 64. Pseudo-depth = 2.56–51.2 m. Average sensitivity value = 0.76. B2) ERT 2–3. Model layers = 16. Model blocks = 1264. Datum points = 627. Electrodes = 80. Pseudo-depth = 2.56–38.4 m. Average sensitivity value = 0.90. B3) ERT-4. Model layers = 14. Model blocks = 330. Datum points = 144. Electrodes = 31. Pseudo-depth = 2.56–25.6 m. Average sensitivity value = 0.78.





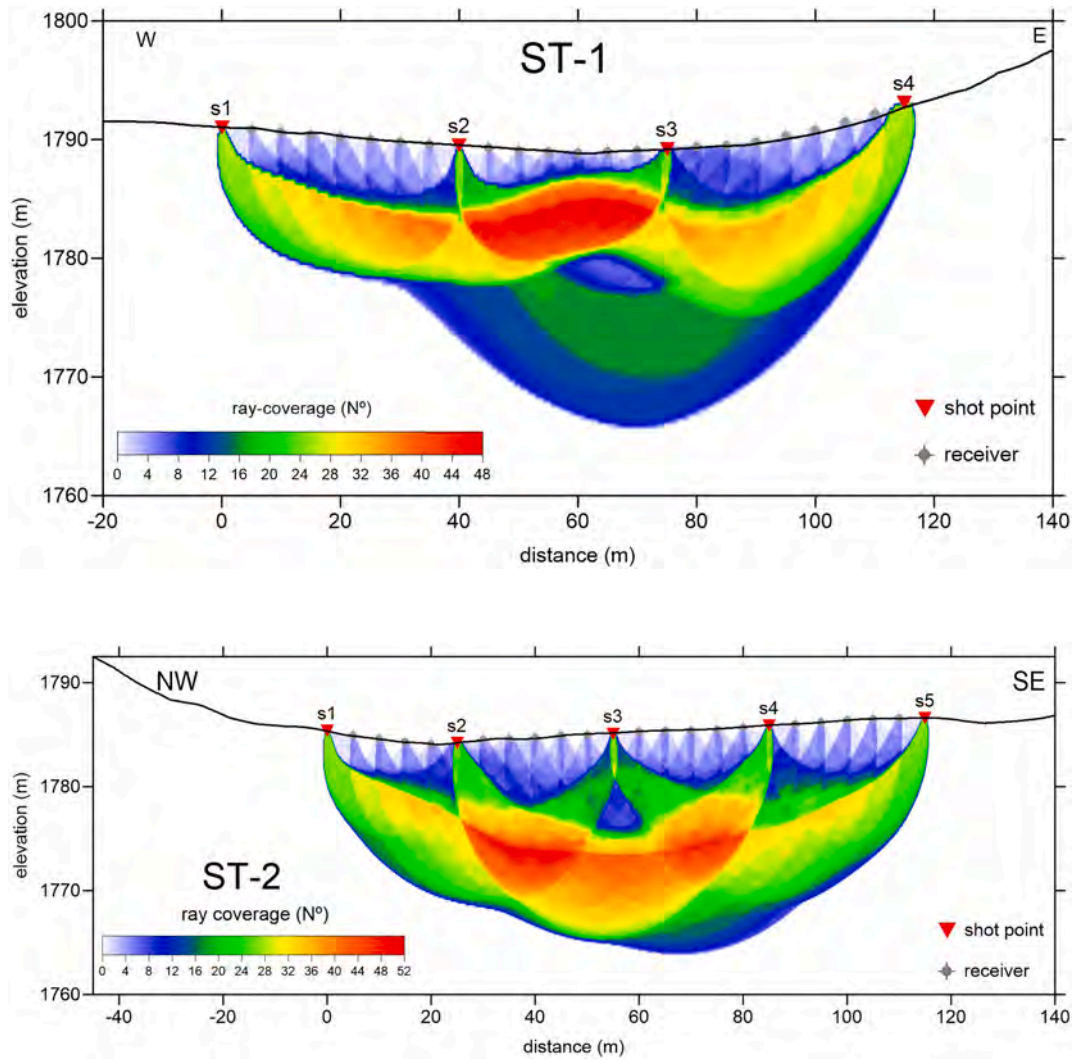
### Appendix C

Examples of stacked shot gathers from active seismic experiment (ST). See location in Fig. 2A. Digital records were pre-processed with standard bandpass filtering and gain enhancement. Red lines show picked travel times. C1) End-on reverse shot in Profile ST-1. C2) Intermediate split-spread shot located in geophone number 18 in Profile ST-2. In this case there is significant energy absorption and attenuation, which makes difficult to identify the first arrival.



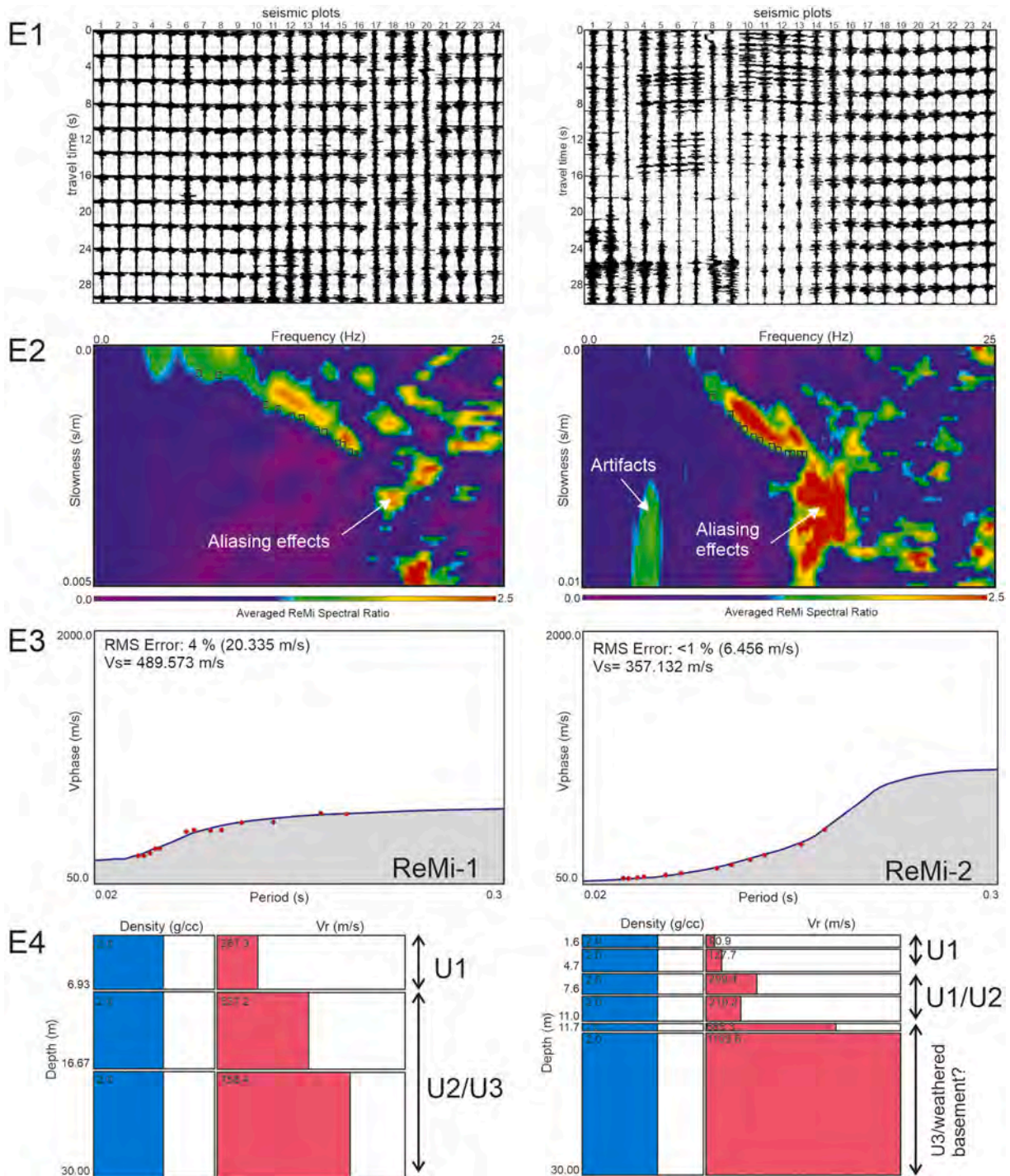
### Appendix D

Ray-tracing coverage of the P-wave tomography inversion. S = Shot point. N° = Number of rays. See location in Fig. 2A. D1) ST-1. D2) ST-2.



**Appendix E**

Refraction Microtremor: ReMi-1 (left) and ReMi-2 (right). See location in Fig. 2A. E1) Seismic records. 24 channels and 30 s-long time window. The seismic source was the natural noise, the percussion with a 6 kg hammer along the geophone array and the signal generated by a DPSH system (mostly periodic events). E2) Slowness-frequency spectrum. Squares show the dispersion picks. E3) Dispersion graphic. Red dots show pairs phase velocity vs. period. Purple line shows the adjusted model.  $V_s$  = average S-velocity up to 30 m of depth. E4) 1D inverted model ( $V_R$  vs. depth). Assumed constant density of 2 g/cc.





## References

- Acaso, E., 1983. Estudio del Cuaternario en el Macizo Central de Gredos (PhD. Thesis). Alcalá de Henares Univ., Spain (442 pp.).
- AEMET/IPMA, 2011. Atlas Climático Ibérico/Iberian Climate Atlas. Agencia Estatal de Meteorología (AEMET) and Instituto Português do Mar e da Atmosfera (IPMA), Madrid. <http://www.aemet.es/divulgacion/publicaciones/>.
- Bobachev, A.A., Shevniin, V.A., Modin, I.N., 2003. IPI2WIN version 3.0.1e. <http://geophysics.geol.msu.ru/ipi2win.htm>.
- Bordonau, J., 1992. Els Complexos glàcio-lacustres relacionats amb el darrer cicle glacial als Pirineus (PhD. Thesis). Barcelona Univ., Spain (294 pp.).
- Bottari, C., Aringoli, D., Carluccio, R., Castellano, C., Caracciolo, F.A., Gasperini, M., Materazzi, M., Nicolosi, I., Pambianchi, G., Pieruccini, P., Sepe, V., 2017. Geomorphological and geophysical investigations for the characterization of the Roman Carsulae site (Tiber basin, Central Italy). *J. Appl. Geophys.* 143, 74–85. <https://doi.org/10.1016/j.jappgeo.2017.03.021>.
- Braucher, R., Bourlès, D., Merchel, S., Vidal Romani, J., Fernandez-Mosquera, D., Marti, K., Léanni, L., Chauvet, F., Arnold, M., Aumaître, G., Keddadouche, K., 2013. Determination of muon attenuation lengths in depth profiles from in situ produced cosmogenic nuclides. *Nucl. Instrum. Methods Phys. Res., Sect. B* 294, 484–490. <https://doi.org/10.1016/j.nimb.2012.05.023>.
- Butler, D.K., 2005. What is near-surface geophysics? In: Butler, D.K. (Ed.), *Near-Surface Geophysics, Investigation in Geophysics N°3*, pp. 1–6. <https://doi.org/10.1190/1.9781560801719.ch1>.
- Cardarelli, E., De Donno, G., 2019. Advances in electric resistivity tomography: theory and case studies. In: Perisco, R., Piro, S., Linford, N. (Eds.), *Innovation in Near-Surface Geophysics*. Elsevier. <https://doi.org/10.1016/C2016-0-03364-8> (517 pp.).
- Carrasco, R.M., Pedraza, J., 1991. Historia morfolodinámica de la Falla de Plasencia en el Valle del Jerte. In: de Gredos, Actas (Ed.), *V Jornadas de Verano de La Sierra de Gredos*, vol. 11. Boletín Universitario, UNED, Ávila, pp. 17–30.
- Carrasco, R.M., Sánchez, J., Muñoz-Martín, A., Pedraza, J., Olaiz, A.J., Ruiz-Zapata, B., Abel-Schaad, D., Merlo, O., Domínguez-Villar, D., 2015a. Caracterización de la geometría de la depresión de Navamundo (Sistema Central Español) aplicando técnicas geofísicas. *Geogaceta* 57, 39–42. <http://www.sociedadgeologica.es/archivos/geogacetas/geo57/G57art10.pdf>.
- Carrasco, R.M., Pedraza, J., Domínguez-Villar, D., Willenbring, J.K., Villa, J., 2015b. Sequence and chronology of the Cuerpo de Hombre paleoglaciar (Iberian Central System) during the last glacial cycle. *Quat. Sci. Rev.* 129, 163–177. <https://doi.org/10.1016/j.quascirev.2015.09.021>.
- Carrasco, R.M., Turu, V., Pedraza, J., Muñoz-Martín, A., Ros, X., Sánchez, J., Ruiz-Zapata, B., Olaiz, A.J., Herrero-Simón, R., 2018. Near surface geophysical analysis of the Navamundo depression (Sierra de Béjar, Iberian Central System): Geometry, sedimentary infill and genetic implications of tectonic and glacial footprint. *Geomorphology* 315, 1–16. <https://doi.org/10.1016/j.geomorph.2018.05.003>.
- Carrasco, R.M., Soteres, R.L., Pedraza, J., Fernández-Lozano, J., Turu, V., López-Sáez, J. A., Karampaglidis, T., Granja-Bruña, J.L., Muñoz-Martín, A., 2020. Glacial geomorphology of the High Gredos Massif: Gredos and Pinar valleys (Iberian Central System, Spain). *J. Maps*. <https://doi.org/10.1080/17445647.2020.1833768>.
- Centeno, J.D., Brell, J.M., 1987. Características de las alteraciones de las Sierras de Guadarrama y Malagón (Sistema Central Español). *Cuaderno Lab. Xeológico Laxe* 12, 79–87. <http://www.iux.es/?page=5&serie=1>.
- Colomero, C., Comina, C., Gianotti, F., Sambuelli, L., 2014. Waterborne and on-land electrical surveys to suggest the geological evolution of a glacial lake in NW Italy. *J. Appl. Geophys.* 105, 191–202. <https://doi.org/10.1016/j.jappgeo.2014.03.020>.
- Cunha, P.P., Martins, A.A., Gomes, A., Stokes, M., Cabral, J., Lopes, F.C., Pereira, D., de Vicente, G., Buylaert, J.-P., Murray, A.S., Antón, L., 2019. Mechanisms and age estimates of continental-scale endorheic to exorheic drainage transition: Douro River, Western Iberia. *Glob. Planet. Chang.* 181, 102985. <https://doi.org/10.1016/j.gloplacha.2019.102985>.
- De Vicente, G., Cunha, P., Muñoz-Martín, A., Cloetingh, S., Olaiz, A., Vegas, R., 2018. The Spanish-Portuguese central system: an example of intense intraplate deformation and strain partitioning. *Tectonics* 37, 4444–4469. <https://doi.org/10.1029/2018TC005204>.
- Domínguez-Villar, D., Carrasco, R.M., Pedraza, J., Cheng, H., Edwards, R.L., Willenbring, J.K., 2013. Early maximum extent of paleoglaciers from Mediterranean mountains during the last glaciation. *Sci. Rep.* <https://doi.org/10.1038/srep02034>.
- Everett, M.E., 2013. *Near-Surface Applied Geophysics*. Cambridge University Press (415 pp.).
- GEODE, 2004. Continuos Digital Geological Mapping. 1:50.000. Instituto Geológico y Minero de España (IGME). <http://info.igme.es/cartografiadigital/geologica/Geode.aspx>.
- Kruse, S., 2013. Near-surface geophysics in geomorphology. In: Bishop, M.P. (Ed.), *Treatise on Geomorphology, Remote Sensing and GIScience in Geomorphology*, vol. 3. Academic Press, San Diego, CA, pp. 103–129.
- Kvamme, K.L., Ernenwein, E.G., Menzer, J.G., 2019. Putting it all together: geophysical data integration. In: Perisco, R., Piro, S., Linford, N. (Eds.), *Innovation in Near-Surface Geophysics*. Elsevier. <https://doi.org/10.1016/C2016-0-03364-8> (517 pp.).
- Legchenko, A., 2007. MRS measurements and inversion in presence of EM noise. *Boletín Geológico y Minero de España* 118 (3), 489–508.
- Legchenko, A., Valla, P., 2002. A review of the basic principles for proton magnetic resonance sounding measurements. *J. Appl. Geophys.* 50, 3–19.
- Loke, M.H., Chambers, J.E., Rucker, D.F., Kuras, O., Wilkinson, P.B., 2013. Recent developments in the direct-current geoelectrical imaging method. *J. Appl. Geophys.* 95, 135–156.
- López-Sáez, J.A., Abel-Schaad, D., Pérez-Díaz, S., Blanco-González, A., Alba-Sánchez, F., Dorado, M., Ruiz-Zapata, B., Gil-García, M.J., Gómez-González, C., Franco-Múgica, F., 2014. Vegetation history, climate and human impact in the Spanish Central System over the last 9000 years. *Quat. Int.* 353, 98–122.
- López-Sáez, J.A., Carrasco, R.M., Turu, V., Ruiz-Zapata, B., Gil-García, M.J., Luelmo-Lautenschlaeger, R., Pedraza, J., 2020. Late Glacial-early holocene vegetation and environmental changes in the western Iberian Central System inferred from a key site: the Navamundo record, Béjar range (Spain). *Quat. Sci. Rev.* 230, 106167. <https://doi.org/10.1016/j.quascirev.2020.106167>.
- Louie, J.N., 2001. Faster, Better: shear-wave velocity to 100 meters depth from Refraction Microtremor arrays. *Bull. Seismol. Soc. Am.* 91, 347–364.
- Martínez de Pisón, E., Muñoz-Jiménez, J., 1972. Observaciones sobre la morfología del Alto Gredos. *Estudios Geográficos* 33 (129), 597–690.
- Milson, J., Eriksen, A., 2011. *Field Geophysics*, 4th ed. John Wiley & Sons, Ltd. (287 pp.).
- Molina-Ballesteros, E., García-González, M.T., Espejo, R., 1991. Study of Paleoweathering on the Spanish Hercynian basement Montes de Toledo (Central Spain). *Catena* 18, 345–354.
- Molina-Ballesteros, E., García-Talegón, J., Vicente-Hernández, M.A., 1997. Palaeoweathering profiles developed on the Iberian Hercynian basement and their relationship to the oldest tertiary surface in central and western Spain. *Geol. Soc. London Spec. Publ.* 120, 175–185.
- Muñoz, J., Palacios, D., Marcos, J., 1995. The influence of the geomorphologic heritage on present slope dynamics. *The Gredos Cirque, Spain. Pirineos* 145–503 146 (c), 35–63.
- Muñoz-Salinas, E., Castillo, M., Sanderson, D., Kinnaird, T., 2013. Unraveling paraglacial activity on Sierra de Gredos, Central Spain: a study based on geomorphic markers, stratigraphy and OSL. *Catena* 110, 207–214. <https://doi.org/10.1016/j.catena.2013.06.018>.
- Novo, Fernández Chicarro, P., 1949. *Diccionario de voces usadas en geografía física*. In: *Real Sociedad Geográfica*, 4<sup>o</sup> (409 pp.).
- Oliva, M., Palacios, D., García-Ruiz, J.M., Andrés, N., Carrasco, R.M., Pedraza, J., Pérez-Alberti, A., Valcárcel, M., Hughes, P.D., 2019. Late Quaternary glacial phases in the Iberian Peninsula. *Earth-Sci. Rev.* 192, 564–600. <https://doi.org/10.1016/j.earscirev.2019.03.015>.
- Palacios, D., de Marcos, J., Vázquez-Selem, L., 2011. Last Glacial Maximum and deglaciation of Sierra de Gredos, Central Iberian Peninsula. *Quat. Int.* 233 (1), 16–26. <https://doi.org/10.1016/j.quaint.2010.04.029>.
- Palacios, D., Andrés, N., Marcos, J., Vázquez-Selem, L., 2012. Maximum glacial advance and deglaciation of the Pinar Valley (Sierra de Gredos, Central Spain) and its significance in the Mediterranean context. *Geomorphology* 177–178, 51–61. <https://doi.org/10.1016/j.geomorph.2012.07.013> 522.
- Pedraza, J., 1994. *Sistema central*. In: Gutiérrez Elorza, M. (Ed.), *Geomorfología de España*. Rueda, Spain, pp. 63–100.
- Pedraza, J., Carrasco, R.M., 2005. El glaciario pleistoceno del Sistema Central. *AEPECT* 13 (3), 278–288. <https://www.raco.cat/index.php/ECT/issue/view/7520>.
- Pedraza, J., Carrasco, R.M., Domínguez-Villar, D., Willenbring, J.K., 2011. Late Pleistocene Glacial Evolutionary Stages in the Spanish Central System. XVIII INQUA, Abstract, ID 1438. *Quat. Int.* 2012, 279–280, 371–372, Bern, Switzerland. <http://www.inqua2011.ch/>.
- Pedraza, J., Carrasco, R.M., Domínguez-Villar, D., Villa, J., 2013. Late Pleistocene glacial evolutionary stages in the Gredos Mountains (Iberian Central System). *Quat. Int.* 302, 88–100. <https://doi.org/10.1016/j.quaint.2012.10.038>.
- Pèlachs, A., Julià, R., Pérez-Obiol, R., Burjachs, F., Expósito, I., Yll, R., Vizcaino, A., Turu, V., Soriano, J.M., 2011. Dades paleoambientals del complex glaciolacustre de l'estany de Burg durant el Tardiglacial (Vall Ferrera, Pallars Sobirà). In: Turu, V., Constante, A. (Eds.), *Simposio de Glaciario: El Cuaternario en España y áreas afines*, Avances en 2011. Fundació Marcel Chevalier - AEQUA, Andorra la Vella, pp. 40–50.
- de Pisón, Martínez, Palacios, E., 1997. Significado del episodio glacial en la evolución morfológica y en el paisaje de la Sierra de Gredos, Sistema Central. In: Gómez Ortiz, A., Pérez Alberti, A. (Eds.), *Las huellas glaciares de las montañas españolas*. Santiago de Compostela, pp. 163–207.
- Plata, J.L., Rubio, F.M., 2008. The use of MRS in the determination of hydraulic transmissivity: the case of alluvial aquifers. *J. Appl. Geophys.* 66, 128–139.
- Reitner, J.M., Gruber, W., Römer, A., Morawetz, R., 2010. Alpine overdeepenings and paleo-ice flow changes: an integrated geophysical-sedimentological case study from Tyrol (Austria). *Swiss J. Geosci.* 103, 385–405. <https://doi.org/10.1007/s00015-010-0046-9>.
- van Rensbergen, P., de Batist, M., Beck, Ch., Manalt, F., 1998. High-resolution seismic stratigraphy of late Quaternary fill of Lake Anney (northwestern Alps): evolution from glacial to interglacial sedimentary processes. *Sediment. Geol.* 117, 71–96.
- van Rensbergen, P., de Batist, M., Beck, Ch., Chapron, E., 1999. High-resolution seismic stratigraphy of glacial to interglacial fill of a deep glacial lake: lake Le Bourget, Northwestern Alps, France. *Sediment. Geol.* 128, 99–129.
- Reynolds, J.M., 2011. *An Introduction to Applied and Environmental Geophysics*, 2nd ed. Wiley-Blackwell, Chichester, UK. (696 pp.).
- Rubio, J.C., Pedraza, J., Carrasco, R.M., 1992. Reconocimiento de tills primarios en el sector central de la Sierra de Gredos (Sistema Central Español). In: Bermúdez, López, et al. (Eds.), *Estudios de Geomorfología en España*, I. SEG, Murcia, pp. 413–422.
- Rubio Sánchez-Aguililla, F.M., Ramiro-Camacho, A., Ibarra Torre, P., 2017. Métodos geofísicos en entornos naturales protegidos. *Tomografía eléctrica*. *Bol. Geol. Min.* 128 (1), 171–192. ISSN: 0366-0176. [10.21701/bolgeomin.128.1.010](https://doi.org/10.21701/bolgeomin.128.1.010).
- Ruiz, P., Gabaldón, V., 1981. Mapa Geológico de Bohoyo. Map 577. Instituto Geológico y Minero de España (IGME), Madrid, Spain. <http://www.igme.es/>.
- Ruiz-Zapata, M.B., Acaso-Deltell, E., 1981. Contribución al estudio del cuadro vegetal climático durante el Cuaternario reciente en el Macizo Central de Gredos, (Ávila). *Bol. R. Soc. Esp. Hist. Nat. Sección geológica* 79 (3–4), 299–307.

- Schrott, L., Hördt, A., Dikau, R. (Eds.), 2003. Geophysical applications in geomorphology. *Z. Geomorphol. Suppl.* 132, 190S.
- Schuster, G.T., Quintus-Bosz, A., 1993. Wavepath eikonal travelttime inversion: theory. *Geophysics* 58, 1314–1323. <https://doi.org/10.1190/1.1443514>.
- Turu, V., 1999. Aplicación de diferentes técnicas geofísicas y geomecánicas para el diseño de una prospección hidrogeológica de la cubeta de Andorra, (Pirineo Oriental): implicaciones paleohidrogeológicas en el contexto glacial andorrano. Actualidad de las técnicas geofísicas aplicadas en hidrogeología. ITGE-IGME, Madrid, Spain, pp. 203–210.
- Turu, V., Boulton, G.S., Ros, X., Peña-Monne, J.L., Marti-Bono, C., Bordonau, J., Serrano-Cañadas, E., Sancho-Marcén, C., Constante-Orríos, A., Pous, J., Gonzalez-Trueba, J. J., Palomar, J., Herrero-Simón, R., García-Ruiz, J.M., 2007. Structure des grands bassins glaciaires dans le nord de la Péninsule Ibérique: comparaison entre les vallées d'Andorre (Pyrénées Orientales), du Gállego (Pyrénées Centrales) et du Trueba (Chaîne Cantabrique). *Quaternaire* 18, 309–325.
- Turu, V., Carrasco, R.M., Pedraza, J., Ros, X., Ruiz-Zapata, B., Soriano-López, J.M., Mur-Cacuo, E., Pélachs-Mañosa, A., Muñoz-Martín, A., Sánchez, J., Echeverría-Moreno, A., 2018. Late glacial and post-glacial deposits of the Navamuño peatbog (Iberian Central System): chronology and paleoenvironmental implications. *Quat. Int.* 470, 82–95.
- Vilaplana, J.M., Casas, A., 1983. Las cubetas de sobreexcavación glacial de Bono y Barruera (Alta Ribagorça, Pirineo Central). *Cuad. Lab. Xeol. Laxe* 6, 283–309.
- Villamor, P., Capote, R., Stirling, M.W., Tsige, M., Berryman, K.R., Martínez-Díaz, J.J., Martín-González, F., 2012. Contribution of active faults in the intraplate area of Iberia to seismic hazard: the Alentejo-Plasencia fault. *J. Iber. Geol.* 38, 85–111.
- Vouillamoz, J.M., Chatenoux, B., Mathieu, F., Baltassat, J.M., Legchenko, A., 2007. Efficiency of joint use of MRS and VES to characterize coastal Aquifer in Myanmar. *J. Appl. Geophys.* 61, 142–154. <https://doi.org/10.1016/j.jappgeo.2006.06.003>.
- Yamakawa, Y., Kosugi, K., Masaoka, N., Sumida, J., Tani, M., Mizuyama, T., 2012. Combined geophysical methods for detecting soil thickness distribution on a weathered granitic hillslope. *Geomorphology* 145–146, 56–69.
- Yaramanci, U., Hertrich, M., 2007. Inversion of magnetic resonance sounding data. *Bol. Geol. Min.* 118 (3), 473–488. [https://www.igme.es/Boletin/2007/118\\_3\\_2007/ART.%204.pdf](https://www.igme.es/Boletin/2007/118_3_2007/ART.%204.pdf).
- Yaramanci, U., Hertrich, M., 2009. Magnetic resonance sounding. In: Kirsch, R. (Ed.), *Groundwater Geophysics*, pp. 253–273.
- Zohdy, A.A.R., 1989. A new method for automatic interpretation of Schlumberger and Wenner sounding curves. *Geophysics* 54, 244–253.